



HAL
open science

Topological sensitivity-based analysis and optimization of microstructured interfaces

Marie Touboul, Rémi Cornaggia, Cédric Bellis

► **To cite this version:**

Marie Touboul, Rémi Cornaggia, Cédric Bellis. Topological sensitivity-based analysis and optimization of microstructured interfaces. 2024. hal-04180360v2

HAL Id: hal-04180360

<https://hal.science/hal-04180360v2>

Preprint submitted on 27 Feb 2024

HAL is a multi-disciplinary open access archive for the deposit and dissemination of scientific research documents, whether they are published or not. The documents may come from teaching and research institutions in France or abroad, or from public or private research centers.

L'archive ouverte pluridisciplinaire **HAL**, est destinée au dépôt et à la diffusion de documents scientifiques de niveau recherche, publiés ou non, émanant des établissements d'enseignement et de recherche français ou étrangers, des laboratoires publics ou privés.

1 TOPOLOGICAL SENSITIVITY-BASED ANALYSIS AND 2 OPTIMIZATION OF MICROSTRUCTURED INTERFACES*

3 MARIE TOUBOUL[†], RÉMI CORNAGGIA[‡], AND CÉDRIC BELLIS[§]

4 **Abstract.** This paper concerns the optimization of microstructures within a surface when
5 considering the propagation of scalar waves across a periodic row of inclusions embedded within a
6 homogeneous matrix. The approach relies on the low-frequency homogenized model, which consists,
7 in the present case, in some effective jump conditions through a discontinuity within the ambient
8 medium. The topological derivatives of the effective parameters defining these jump conditions are
9 computed from an asymptotic analysis. Their expressions are validated numerically and then used
10 to study the sensitivity of the homogenized model to the geometry in the case of elliptic inclusions.
11 Finally, a topological optimization algorithm is used to minimize a given cost functional. This relies
12 on the expression of the topological derivatives to iteratively perform phases changes in the unit cell
13 characterizing the material, and on FFT-accelerated solvers previously adapted to solve the band cell
14 problems underlying the homogenized model. To illustrate this approach, the resulting procedure is
15 applied to the design of a microstructure that minimizes transmitted fields along a given direction.

16 **Key words.** topological optimization, asymptotic methods, periodic media, microstructured
17 interfaces, effective jump conditions

18 **1. Introduction.** The design of microstructured media allows to control wave
19 propagation and may lead to exotic effects, e.g. negative refraction, subwavelength
20 imaging, lensing and cloaking, to cite a few. It constitutes the paradigm of meta-
21 materials, which have undergone spectacular developments since the early 2000: see
22 [19] and references therein for an overview. An active direction of research concerns
23 the size reduction of microstructures to design compact metamaterial devices. It is
24 indeed advantageous to replace a volumic distribution by a surfacic (in 3D) or a lineic
25 (in 2D) distribution of scatterers, often called metasurface [10] or meta-interface [27].

26 The two-scale homogenization method is a privileged tool to derive formally an
27 approximate model for wave propagation in microstructured media [12, 44]. It avoids
28 having to mesh fine spatial scales and gives an analytical insight on the macroscopic
29 behaviour of waves. However, the usual homogenization methods in the bulk fail
30 when considering a thin row of scatterers, because of boundary effects at the tran-
31 sition between the scatterers and the homogenous medium in which it is embedded.
32 To recover their efficiency, these methods must then be combined with matched as-
33 ymptotic expansions [29], yielding effective jump conditions on an equivalent meta-
34 interface [21, 31, 20, 30, 42].

35 In the context of metamaterials, the optimization of microstructures is a useful
36 tool to determine designs that exhibit interesting macroscopic behaviours. To this
37 purpose, different types of optimization can be considered: (i) the *parametric* opti-
38 mization when the shapes are parameterised by a fixed number of variables (thickness,
39 dimensions, etc.); (ii) the *shape* optimization [1] when, from an initial shape, the posi-
40 tion of the boundaries of the microstructure is changed without changing its topology;
41 (iii) the *topological* optimization [11] when the best possible geometry is sought, even
42 if it means changing the topology. In this work, we are interested in topological opti-

*Submitted to the editors DATE.

[†]UMI 2004 Abraham de Moivre-CNRS, Department of Mathematics, Imperial College London, London SW7 2AZ, UK (m.touboul@imperial.ac.uk).

[‡]Sorbonne Université, CNRS, UMR 7190, Institut Jean Le Rond d'Alembert, F-75005 Paris, France (remi.cornaggia@sorbonne-universite.fr).

[§]Aix Marseille Univ, CNRS, Centrale Marseille, LMA, Marseille, France (bellis@lma.cnrs-mrs.fr).

43 mization which leaves more freedom compared to the first two methods. The chosen
 44 mathematical tool to perform this type of optimization is the *topological derivative*
 45 [7, 38] which measures the sensitivity of a cost functional to infinitesimal topological
 46 perturbations.

47 Then, different numerical methods can be employed to update the material prop-
 48 erties based on the knowledge of the topological derivatives. One method used in this
 49 paper is the *level-set* method. For a two-phase material, it relies on the characteriza-
 50 tion of the phase distribution thanks to a level-set function which is strictly positive
 51 in one phase and strictly negative in the other phase. This has first been introduced
 52 for *shape* optimization and is based on the fact that the interface between phases,
 53 which corresponds to the zero level-set function, can evolve based on the shape deriv-
 54 ative of the cost functional with respect to a perturbation of this interface [2, 3]. This
 55 methodology has then been adapted to topological perturbation based on a projection
 56 algorithm [8, 9, 24, 39].

57 A strategy for microstructure optimization, in line with the homogenization set-
 58 ting considered in this paper, is to perform the optimization from the homogenized
 59 model that describes the material, an issue often referred to as inverse homogenization
 60 [45]. It relies on the definition of a cost function, to be minimized, in terms of the
 61 effective coefficients that characterize the homogenized model. At low frequency, this
 62 method has been used in statics [9, 25, 39], in dynamics for a low contrast [3, 17],
 63 and a high contrast [49] of the physical properties (activating resonances of the highly
 64 contrasted inclusions). It has also been extended to optimize effective properties at
 65 high frequencies [37].

66 In this framework, a topological optimization procedure is presented in [17] to
 67 optimize dynamical properties for antiplane shear waves based on homogenization.
 68 The main ingredients are the following ones:

- 69 1. the two-scale asymptotic homogenization method is deployed,
- 70 2. a cost functional is constructed from the homogenized model,
- 71 3. its topological derivative is computed,
- 72 4. the cost functional minimization is performed thanks to a level-set algorithm,
- 73 5. the level-set is iterated by computing cell problems using FFT-accelerated
 74 solvers.

75 Noticeably, works on the optimization in dynamics of microstructured thin layers
 76 are more scarce and recent: [32] for an optimization of slabs based on their far-field
 77 behaviour and [36] for a design of acoustic metasurfaces based on a homogenization
 78 model. In the present paper, we perform a sensitivity analysis and the optimization
 79 of an acoustic microstructured interface, based on the homogenized model of [30] and
 80 following the same overall approach as in [17]. The novelties compared to [36] and [17]
 81 are (i) the calculation of topological derivatives and their use *prior to the topological*
 82 *optimization process* to perform a sensitivity analysis of the effective properties and
 83 to determine valuable initializations from the closed-form formula provided by the
 84 topological derivatives for elliptical inclusions; and (ii) the use of non-conventional
 85 FFT-based solvers to address the specific *unbounded* cell problems that arise from the
 86 two-scale homogenization of microstructured interfaces.

87

88 The paper is organized as follows: the homogenized model is recalled in Section 2,
 89 and an analysis of **the** macroscopic observables is performed, leading to the definition
 90 of the considered optimization problem. In Section 3, the topological derivatives of
 91 the effective parameters of the interface model are derived and validated numerically.
 92 Then, in Section 4, based on the analytical information provided by these derivatives,

93 a topological sensitivity-based analysis is performed for microstructures made of el-
 94 liptic inclusions, and “asymptotically optimal” ellipses are determined for the chosen
 95 cost functional. Then a topological optimization scheme, which relies on the topo-
 96 logical derivatives to update the material distribution at each iteration, is presented
 97 in Section 5. We finally summarize the results and discuss possible perspectives in
 98 Section 6.

99 **2. Microstructured interfaces, effective model and optimization prob-** 100 **lem.**

101 **2.1. Setting and homogenization.** Let us consider the propagation of waves
 102 in two dimensions across a periodic row of inclusions $\cup_i \Omega_i$ embedded within a homo-
 103 geneous matrix Ω_m . The thickness and the period of the row are denoted by e and h ,
 104 respectively, and we assume that $e = \mathcal{O}(h)$. The time and the spatial coordinates are
 105 denoted by t and $\mathbf{X} = (X_1, X_2)$, respectively, with X_2 being the direction of period-
 106 icity of the inclusions as shown in Figure 1. Anti-plane elastic waves are considered,
 107 and both media are assumed to be isotropic and homogeneous. The microstructured
 108 medium is therefore characterized by two constitutive parameters, the mass density
 109 ρ_h and the shear modulus μ_h , that are piecewise constant:

$$110 \quad (2.1) \quad (\rho_h, \mu_h)(\mathbf{X}) = \begin{cases} (\rho_m, \mu_m) & \text{in the matrix,} \\ (\rho_i, \mu_i) & \text{in the inclusions,} \end{cases}$$

111 and the time-domain governing equation for the out-of-plane component U_h of the
 112 material displacement reads:

$$113 \quad (2.2) \quad \rho_h(\mathbf{X}) \frac{\partial^2 U_h}{\partial t^2}(\mathbf{X}, t) = \nabla \cdot (\mu_h(\mathbf{X}) \nabla U_h(\mathbf{X}, t)) + \rho_m \delta(\mathbf{X} - \mathbf{X}_S) g(t),$$

114 where g is a source term located at a point \mathbf{X}_S in the matrix. Introducing the scalar
 115 velocity field $V_h = \partial U_h / \partial t$ and the stress vector $\Sigma_h = \mu_h \nabla U_h$ gathering the two shear
 116 components of the stress tensor, this system can be rewritten as a first-order system
 117 in time:

$$118 \quad (2.3) \quad \begin{cases} \frac{\partial \Sigma_h}{\partial t}(\mathbf{X}, t) = \mu_h(\mathbf{X}) \nabla V_h(\mathbf{X}, t), \\ \rho_h(\mathbf{X}) \frac{\partial V_h}{\partial t}(\mathbf{X}, t) = \nabla \cdot \Sigma_h(\mathbf{X}, t) + \rho_m \delta(\mathbf{X} - \mathbf{X}_S) g(t), \end{cases}$$

119 with V_h and $\Sigma_h \cdot \mathbf{n}$ being continuous at each matrix/inclusion interface $\partial \Omega_i$, given
 120 that \mathbf{n} is the *inward* unit normal on each $\partial \Omega_i$.

121

122 **In the following time-domain simulations, we will only consider excitations by a**
 123 **source point in a medium initially at rest, ie $V_h(\mathbf{X}, t = 0) = 0$ and $\Sigma_h(\mathbf{X}, t = 0) = \mathbf{0}$.**
 124 **This choice removes the need for studying the small-scale interactions between the**
 125 **initial fields and the microstructure.**

126 *Remark 2.1.* The system (2.3) is also relevant to model other physical phenomena,
 127 such as acoustic waves for which the fields Σ_h , V_h , ρ_h and $1/\mu_h$ would stand instead
 128 for the in-plane particle velocity, acoustic pressure, compressibility and mass density,
 129 respectively.

130 The assumptions of the homogenization process and the results obtained in [30]
 131 are now briefly reminded.

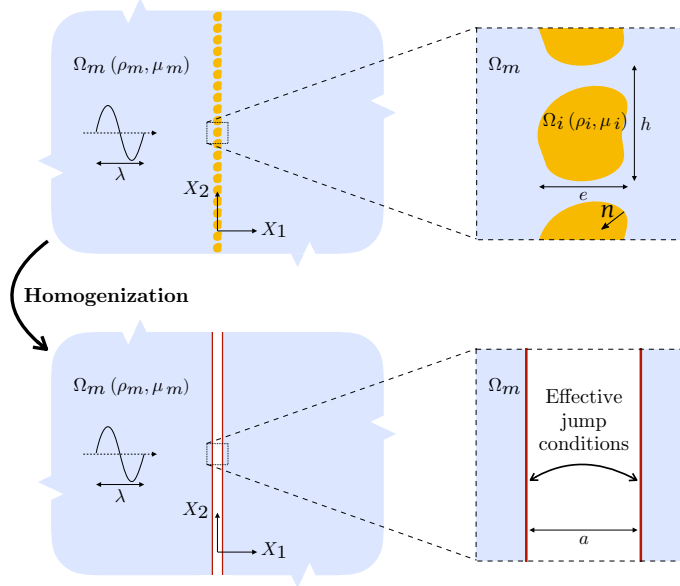


Fig. 1: Homogenization process for a single periodic array of inclusions. *(top)* Original configuration with a thin microstructured layer, *(bottom)* Homogenized interface model.

132 *Hypotheses of the homogenization process.* Considering that the system is excited
 133 by an incident wave or external sources, the characteristic wavelength λ within the
 134 matrix is assumed to be much larger than the period h . Defining the wavenumber
 135 within the matrix as $k_m = 2\pi/\lambda$, we introduce the parameter

$$136 \quad (2.4) \quad \eta = k_m h$$

137 and we assume that $\eta \ll 1$ for the configurations of interest.

138 Throughout this article, only the *non-resonant* case is addressed, i.e. the physical
 139 parameters of the matrix and of the inclusions are supposed to be of the same order
 140 of magnitude. For large contrasts, e.g. for very soft but dense inclusions ($\mu_i \ll \mu_m$
 141 and $\rho_i \sim \rho_m$), the resonances of these inclusions play a key role in the transmission of
 142 waves, and should be captured by specific homogenization methods, see e.g. [42, 48]
 143 and the references therein.

144 These geometrical and material assumptions allow to homogenize the microstruc-
 145 ture in the so-called long-wavelength, non-resonant regime.

146 *Notations.* The so-called fast scale of coordinates is $\mathbf{y} = \mathbf{X}/h = (y_1, y_2)^\top$. The
 147 domain Ω is the elementary cell $\mathbb{R} \times [-1/2, 1/2]$ in \mathbf{y} -coordinates, see Figure 2, that
 148 is repeated periodically in the y_2 direction to obtain the full domain, and $(\mathbf{e}_1, \mathbf{e}_2)$ is
 149 the canonical basis of \mathbb{R}^2 . For any function $f(x_1)$, we define the jump and the mean
 150 value around the (centered) enlarged interface of thickness a :

$$151 \quad (2.5) \quad \llbracket f \rrbracket_a = f(a/2) - f(-a/2) \quad \text{and} \quad \langle f \rangle_a = \frac{1}{2}(f(a/2) + f(-a/2)).$$

152 We will also make use of the relative material constrasts τ^μ and τ^ρ defined by:

$$153 \quad (2.6) \quad \tau^\mu = \frac{\mu_i - \mu_m}{\mu_m} \quad \text{and} \quad \tau^\rho = \frac{\rho_i - \rho_m}{\rho_m}.$$

154 *Cell problems.* The homogenization process requires the computation of auxiliary
155 fields Φ_j for $j = 1, 2$ which are solutions of *band cell problems*. The problems initially
156 proposed by [30] were posed on the semi-infinite representative cell Ω . For practical
157 implementation, the authors of the present paper proposed in [18] a reformulation on
158 a bounded rectangular cell Ω^a defined by:

$$159 \quad (2.7) \quad \Omega^a = \left[-\frac{a}{2h}; \frac{a}{2h} \right] \times \underbrace{\left[-\frac{1}{2}; \frac{1}{2} \right]}_I$$

160 such that the material data set

$$161 \quad (2.8) \quad \mathbf{m}(\mathbf{y}) := (\rho(\mathbf{y}), \mu(\mathbf{y}))$$

162 satisfies

$$163 \quad (2.9) \quad \mathbf{m}(\mathbf{y}) = (\rho_m, \mu_m) \quad \forall \mathbf{y} \in \Omega \setminus \Omega^a,$$

164 as represented in Figure 2. The parameter a used in the choice of the representative
165 cell Ω^a also defines the *effective interface width*, see Figure 1. It should satisfy $a \geq e$
166 to ensure that the material variations are retrained to Ω^a , and for the effective model
167 presented below to satisfy some stability conditions [30].

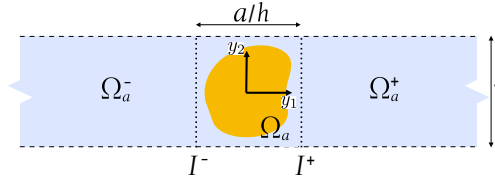


Fig. 2: Elementary cell Ω , decomposed into the bounded cell Ω^a , and half strips $\Omega_a^+ = [\frac{a}{2h}, +\infty[\times I^+$ and $\Omega_a^- =]-\infty, -\frac{a}{2h}] \times I^-$, with $I^\pm = \{(y_1, y_2) \in \Omega_a^\pm, y_1 = \pm \frac{a}{2h}\}$.

168 Using the notation $\Phi = (\Phi_1, \Phi_2)$ for compactness, two (uncoupled) band cell
169 problems are defined as:

$$170 \quad (2.10) \quad \begin{cases} \nabla \cdot (\mu(\mathbf{y}) (\nabla \Phi + \mathbf{I}_2)) = \mathbf{0} \text{ in } \Omega^a, \\ \Phi \text{ is } y_2\text{-periodic,} \\ \partial_n \Phi \left(\pm \frac{a}{2h}, \cdot \right) = \mathbf{\Lambda} \left(\Phi \left(\pm \frac{a}{2h}, \cdot \right) \right) \text{ on } I^\pm, \end{cases}$$

171 where \mathbf{I}_2 is the second-order identity tensor, (I^-, I^+) are the left and right boundaries
172 of Ω^a (see Figure 2) and $\mathbf{\Lambda}$ is a nonlocal *Dirichlet-to-Neumann* (DtN) operator, see
173 [26, 15, 18] and the expression recalled in Appendix A for completeness. In (2.10) and
174 hereafter, the adopted convention for the gradient components is such that $(\nabla \Phi)_{ij} =$
175 $\partial \Phi_j / \partial y_i$.

176 These elementary solutions will serve to compute the effective parameters that
177 appear in the homogenized model presented now.

178 *Homogenized model.* From [30], we know that the homogenization of the problem
 179 (2.3) at order $\mathcal{O}(\eta)$ in such a configuration yields the following homogenized model
 180 for the first-order approximation (V, Σ) of (V_h, Σ_h) :

$$(2.11) \quad \begin{cases} \frac{\partial \Sigma}{\partial t}(\mathbf{X}, t) = \mu_m \nabla V(\mathbf{X}, t) & (|X_1| \geq a/2, X_2 \in \mathbb{R}), \\ \rho_m \frac{\partial V}{\partial t}(\mathbf{X}, t) = \nabla \cdot \Sigma(\mathbf{X}, t) + \rho_m \delta(\mathbf{X} - \mathbf{X}_S)g(t) & (|X_1| \geq a/2, X_2 \in \mathbb{R}), \\ \llbracket V \rrbracket_a = h \left\{ \mathcal{B} \left\langle \frac{\partial V}{\partial X_1} \right\rangle_a + \mathcal{B}_2 \left\langle \frac{\partial V}{\partial X_2} \right\rangle_a \right\} & (X_2 \in \mathbb{R}), \\ \llbracket \Sigma_1 \rrbracket_a = h \left\{ \mathcal{S} \langle \nabla \cdot \Sigma \rangle_a - \mathcal{C}_1 \left\langle \frac{\partial \Sigma_1}{\partial X_2} \right\rangle_a - \mathcal{C} \left\langle \frac{\partial \Sigma_2}{\partial X_2} \right\rangle_a \right\} & (X_2 \in \mathbb{R}), \end{cases}$$

182 featuring imperfect transmission conditions for the velocity V and normal component
 183 of the stress vector $\Sigma_1 = \Sigma \cdot \mathbf{e}_1$. **This system will be studied both in the time domain,**
 184 **where the same source point and null initial conditions than in the microstructured**
 185 **problem will be used, and in the time-harmonic regime for an established incident**
 186 **plane wave, see Section 2.2 below.**

187 The *effective coefficients* entering the **transmission** conditions are the parameter

$$(2.12) \quad \mathcal{S} = \frac{a}{h} + \tau^\rho |\Omega_i|$$

189 where $|\Omega_i| = \int_{\Omega_i} d\mathbf{y}$ is the surface of the inclusion phase in the rescaled coordinates,
 190 and the four coefficients $(\mathcal{B}, \mathcal{B}_2, \mathcal{C}_1, \mathcal{C})$, with the notation of [30]. They are gathered
 191 in the two vector-valued parameters $\mathcal{B} = (\mathcal{B}, \mathcal{B}_2)$ and $\mathcal{C} = (\mathcal{C}_1, \mathcal{C})$, and are expressed
 192 in terms of the elementary solution Φ to (2.10) as:

$$(2.13) \quad \mathcal{B}(\mathbf{m}) = \frac{a}{h} \mathbf{e}_1 + \int_I \left[\Phi \left(\frac{a}{2h}, y_2 \right) - \Phi \left(-\frac{a}{2h}, y_2 \right) \right] dy_2,$$

194 and:

$$(2.14) \quad \mathcal{C}(\mathbf{m}) = \int_{\Omega^a} \frac{\mu(\mathbf{y})}{\mu_m} \left(\frac{\partial \Phi}{\partial y_2}(\mathbf{y}) + \mathbf{e}_2 \right) d\mathbf{y}.$$

196 Important properties of the coefficients $(\mathcal{B}_2, \mathcal{C}_1)$ were also proven in [30], namely

- 197 • $\mathcal{B}_2 = -\mathcal{C}_1$ in all cases,
- 198 • $\mathcal{B}_2 = \mathcal{C}_1 = 0$ for the cells that are symmetric with respect to the medium
 199 horizontal plane $y_2 = 0$, see Figure 2 (e.g. for circular inclusions).

200 Finally, the interface energy associated with the homogenized problem (2.11) is proven
 201 to be positive as soon as a is greater than e [30], ensuring stability of the solution
 202 to (2.11). In the harmonic regime, the well-posedness of similar homogenized models
 203 with effective jump conditions has been tackled in [21, 22]. **Instabilities in the time-**
 204 **domain for a system associated to a negative interface energy has been analysed and**
 205 **illustrated in [23].**

206 Hereafter, the effective parameters are collected in \mathbf{m}_{eff} as:

$$(2.15) \quad \mathbf{m}_{\text{eff}} := (\mathcal{B}, \mathcal{B}_2, \mathcal{S}, \mathcal{C}_1, \mathcal{C}).$$

208 **2.2. Analysis of macroscopic observables and optimization problem.** In
 209 this section, the aim is to identify macroscopic effects specific to the microstructured

210 interfaces, described by the homogenized model in the considered long-wavelength
 211 regime. To find an optimal design that would enhance these effects, an optimization
 212 problem should be established. To do so, we use some analytical macroscopic observ-
 213 ables of the homogenized problem, which are the scattering coefficients computed for
 214 incident plane waves **in the time-harmonic regime**, together with observations from
 215 time-domain simulations with point sources. The considered optimization problem is
 216 finally given.

217 **2.2.1. Scattering coefficients for time-harmonic plane waves.** In this sec-
 218 tion, we consider **an established time-harmonic regime at circular frequency ω** . We
 219 **therefore use** the frequency-domain formulation of the **homogenized model (2.11)**
 220 **with $g = 0$** , which is equivalent to the model obtained by applying homogeniza-
 221 tion in the frequency domain, see [48]. **Introducing the amplitude of the time-**
 222 **harmonic wavefield $\hat{\mathbf{U}}(\mathbf{X}, \omega) = (\hat{V}(\mathbf{X}, \omega), \hat{\Sigma}_1(\mathbf{X}, \omega), \hat{\Sigma}_2(\mathbf{X}, \omega))^T$ and its decompo-**
 223 **sition $\hat{\mathbf{U}} = \hat{\mathbf{U}}_I + \hat{\mathbf{U}}_R + \hat{\mathbf{U}}_T$ into incident $\hat{\mathbf{U}}_I$, reflected $\hat{\mathbf{U}}_R$ and transmitted $\hat{\mathbf{U}}_T$ waves,**
 224 **we consider incident plane waves given by:**

$$225 \quad (2.16) \quad \hat{\mathbf{u}}_I(\mathbf{X}, \omega) = \begin{pmatrix} 1/\mu_m \\ -\cos \theta_I/c_m \\ -\sin \theta_I/c_m \end{pmatrix} \exp(-i\mathbf{k}_I \cdot \mathbf{X}),$$

226 with $c_m = \sqrt{\mu_m/\rho_m}$ the celerity of waves in the matrix, θ_I the direction of propagation,
 227 $\mathbf{k}_I = (\omega/c_m)(\cos(\theta_I), \sin(\theta_I))$ the corresponding wavevector.

228 We also look for reflected and transmitted plane waves as:

$$229 \quad (2.17) \quad \begin{cases} \hat{\mathbf{u}}_R(\mathbf{X}, \omega) = \begin{pmatrix} 1/\mu_m \\ -\cos \theta_R/c_m \\ -\sin \theta_R/c_m \end{pmatrix} \exp(-i\mathbf{k}_R \cdot \mathbf{X}) \mathcal{R}(\theta_I, \omega), \\ \hat{\mathbf{u}}_T(\mathbf{X}, \omega) = \begin{pmatrix} 1/\mu_m \\ -\cos \theta_T/c_m \\ -\sin \theta_T/c_m \end{pmatrix} \exp(-i\mathbf{k}_T \cdot \mathbf{X}) \mathcal{T}(\theta_I, \omega). \end{cases}$$

230 Inserting the expression above in the frequency-domain jump conditions, see [47], the
 231 relection and transmission angles are classically found to be $\theta_R = \pi - \theta_I$ and $\theta_T = \theta_I$
 232 (\mathbf{k}_R and \mathbf{k}_T are the corresponding wavevectors with same wavenumber ω/c_m), and
 233 the expression of the reflexion and transmission coefficients \mathcal{R} and \mathcal{T} can be obtained
 234 analytically. They read respectively:

$$235 \quad (2.18) \quad \begin{cases} \mathcal{R}(\theta_I, \omega) = \frac{i\omega \mathcal{L}}{\mathcal{Z} + i\omega \mathcal{N} - \omega^2 \mathcal{M}} \exp\left(i\frac{\omega}{c_m} a \cos \theta_I\right), \\ \mathcal{T}(\theta_I, \omega) = \frac{\mathcal{Z} + i\omega \mathcal{G} + \omega^2 \mathcal{M}}{\mathcal{Z} + i\omega \mathcal{N} - \omega^2 \mathcal{M}} \exp\left(i\frac{\omega}{c_m} a \cos \theta_I\right), \end{cases}$$

236 with $c_m = \sqrt{\mu_m/\rho_m}$ and

$$237 \quad (2.19) \quad \begin{cases} \mathcal{L} = h (\mathcal{B} \cos(\theta_I)^2 + \mathcal{C} \sin(\theta_I)^2 - \mathcal{S}), \\ \mathcal{Z} = 2c_m \cos \theta_I, \\ \mathcal{N} = h (-\mathcal{C} \sin(\theta_I)^2 + \mathcal{B} \cos(\theta_I)^2 + \mathcal{S}), \\ \mathcal{M} = \frac{h^2}{2c_m} (\mathcal{B}_2 \mathcal{C}_1 \sin(\theta_I)^2 - \mathcal{B} \mathcal{C} \sin(\theta_I)^2 + \mathcal{B} \mathcal{S}) \cos(\theta_I), \\ \mathcal{G} = -h(-\mathcal{C}_1 + \mathcal{B}_2) \cos(\theta_I) \sin(\theta_I). \end{cases}$$

238 One can notice a symmetry with respect to the change $\theta_I \rightarrow -\theta_I$ for the reflexion
 239 coefficient $\mathcal{R}(\theta_I, \omega)$ and for the modulus of the transmission coefficient $|\mathcal{T}(\theta_I, \omega)|$.
 240 Consequently, only the argument of the transmission coefficient $\arg(\mathcal{T}(\theta_I, \omega))$ is not
 241 symmetric with respect to the normal incidence. The quantity \mathcal{G} defined in (2.19)
 242 and proportional to $\mathcal{B}_2 = -\mathcal{C}_1$ is responsible for this asymmetry, which is therefore
 243 obtained for cells which are non-symmetric with respect to the horizontal plane $y_2 = 0$.

244 From this observation, we chose to focus on these non-symmetric geometries,
 245 to exhibit and enhance macroscopic effects that would not appear for symmetric
 246 configurations more studied in the literature (say, circular or rectangular inclusions
 247 aligned with the main axes [30]).

Table 1: Physical parameters considered for the microstructure.

μ_i	ρ_i	μ_m	ρ_m
78 GPa	7800 kg · m ⁻³	12 GPa	2500 kg · m ⁻³

248 **2.2.2. Observations from time-domain simulations.** To investigate these
 249 configurations, one considers a microstructure typical of steel in concrete, for which
 250 the physical parameters are given by Table 1. The periodicity length is $h = 1\text{m}$ and the
 251 examples of two geometries for the inclusion Ω_i are investigated: one ellipse of semi-
 252 axes lengths (0.15, 0.5) tilted of $-\pi/4$ and one rectangle of sizes (1.25, 0.08) tilted of
 253 $-\pi/4$. The effective parameters associated to these two configurations are computed
 254 and time-domain simulations are performed in the associated effective media **in a**
 255 **rectangular domain** $\mathbf{X} \in [-70; 35] \times [-132; 132]$.

256 In this part, the considered excitation is **no longer an incident** plane wave but
 257 a source point $\delta(\mathbf{X} - \mathbf{X}_S)g(t)$, with $g(t)$ a sufficiently regular, wide-band signal. Here
 258 we choose g defined as:

$$259 \quad (2.20) \quad g(t) = \begin{cases} A \sum_{m=1}^4 \alpha_m \sin(\beta_m \omega_c t) & \text{if } 0 < t < \frac{1}{f_c}, \\ 0 & \text{otherwise,} \end{cases}$$

260 where $\beta_m = 2^{m-1}$ and the coefficients α_m being $\alpha_1 = 1$, $\alpha_2 = -21/32$, $\alpha_3 = 63/768$,
 261 $\alpha_4 = -1/512$. It entails that $g \in C^6([0, +\infty[)$ and $g(t)$ is a wide-band signal with a
 262 central frequency $f_c = \omega_c/2\pi$. The source is located at $\mathbf{X}_S = (-35, 0)$, with $X_1 = 0$
 263 being the center of the enlarged effective interface. The central frequency is $f_c = 50\text{ Hz}$
 264 which corresponds to a small parameter $\eta = 0.14$ for which a good agreement between
 265 the homogenized model and the microstructured configuration has been observed.
 266 The time-domain simulations are performed thanks to Finite Differences and to the
 267 Explicit Simplified Interface Method [28] to handle the effective enlarged interface.

268
 269 **To highlight the interface contribution, we define and compute the incident fields**
 270 **\mathbf{u}_I as the fields which would propagate in the matrix only (without interface) for this**
 271 **excitation, and introduce the scattered fields $\mathbf{u}_{sc} = (V_{sc}, (\boldsymbol{\Sigma}_{sc})_1, (\boldsymbol{\Sigma}_{sc})_2)^T = \mathbf{u} - \mathbf{u}_I$,**
 272 **which are computed from time $t = 0$ until $t_f = 86.7\text{ ms}$. From these data, one can**
 273 **compute the local cumulative energy defined as:**

$$274 \quad (2.21) \quad \mathcal{E}(\mathbf{X}) = \frac{1}{2} \int_0^{t_f} \left(\frac{1}{\mu_m} \boldsymbol{\Sigma}_{sc}(\mathbf{X}, t)^2 + \rho_m V_{sc}(\mathbf{X}, t)^2 \right) dt.$$

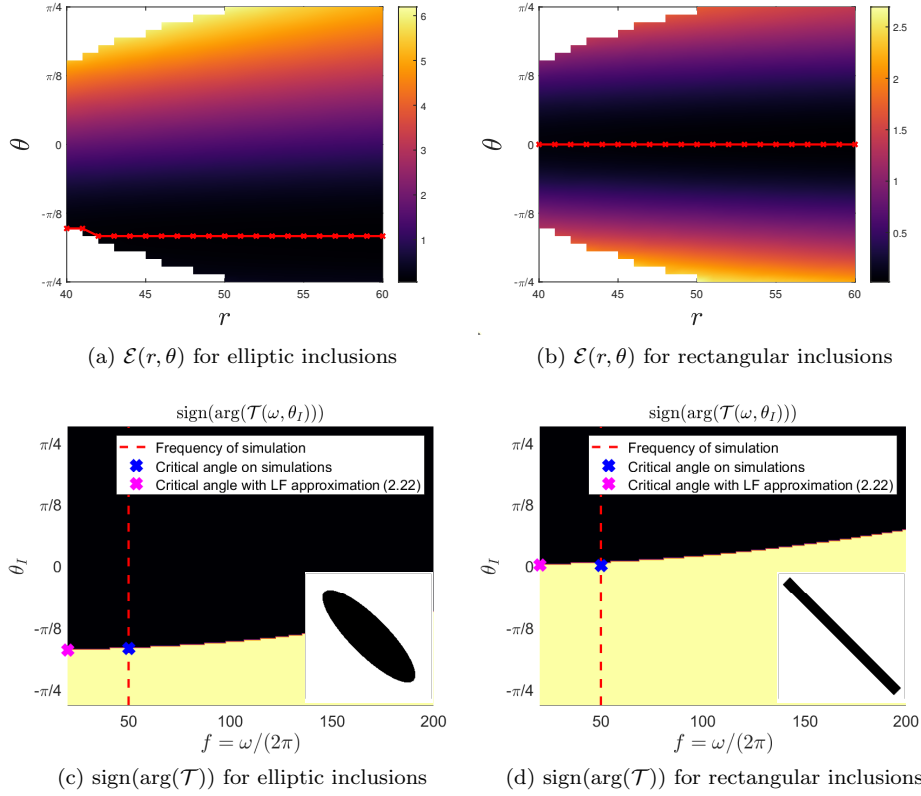


Fig. 3: Cumulative energy in polar coordinates (first row) where the position of the minimal value for a given r is denoted by the red crosses, and study of $\text{sign}(\arg(\mathcal{T}))$ (second row, yellow and black for positive and negative signs, respectively), computed with the effective model corresponding to elliptic (left) and rectangular (right) inclusions.

275 This quantity is evaluated on the right of the interface for both microstructures
 276 Figures 3a and 3b as a function of the polar coordinates (r, θ) centered at \mathbf{X}_S , with
 277 $r \in [40; 60]$. For each value of r , we observe that the energy \mathcal{E} is minimal for a given
 278 angle θ_{\min} , denoted by red crosses. Moreover, one can notice that this value θ_{\min} seems
 279 to be independant of r . Furthermore, the sign of $\arg(\mathcal{T})$ is plotted in Figures 3c and
 280 3d (black and yellow maps where yellow and black stand for positive and negative sign,
 281 respectively) for the same two microstructures directly using the analytical formula
 282 (2.19), as a function of θ_I and ω . It is then observed that this critical value measured
 283 on time-domain simulations (denoted by the blue cross) seems to coincide with the
 284 value of θ_I for which $\arg(\mathcal{T})$ changes sign at low frequency.

285 These observations **suggest** a link between the two characterizations of microstruc-
 286 tured interfaces presented above, namely (i) the effective scattering coefficients com-
 287 puted from the homogenized model and (ii) the angle θ_{\min} of minimal scattered energy,
 288 measured numerically for a circular incident wave. Considering that minimizing the
 289 energy emitted by a known source, in a chosen direction θ_{\min} , is a problem of interest

for e.g. directive sound attenuation, we therefore aim at designing microstructures associated with a vanishing $\arg(\mathcal{T}(\theta_I, \omega))$ for $\theta_I = \theta_{\min}$ and low frequencies.

2.2.3. Optimization problem. To exhibit an analytical link between the critical value θ_{\min} at low frequency and the homogenized coefficients \mathbf{m}_{eff} , one considers a first-order approximation for the transmission coefficient \mathcal{T} . In this low-frequency limit, we consider a fixed geometry and therefore a fixed value of h , while ω , and consequently η , tends to 0. Upon introducing $\bar{\mathcal{G}} = \mathcal{G}/h$, $\bar{\mathcal{M}} = 2c_m \mathcal{M}/h^2$ and $\bar{\mathcal{N}} = \mathcal{N}/h$ in (2.18) and (2.19), this leads to:

$$\begin{aligned} \mathcal{T}(\theta_I, \omega) &= \frac{\mathcal{L} + i\eta c_m \bar{\mathcal{G}} + \eta^2 \frac{c_m}{2} \bar{\mathcal{M}}}{\mathcal{L} + i\eta c_m \bar{\mathcal{N}} - \eta^2 \frac{c_m}{2} \bar{\mathcal{M}}} \exp\left(i\eta \frac{a}{h} \cos(\theta_I)\right) \\ &= \frac{1 + i\eta \frac{\bar{\mathcal{G}}}{2\cos(\theta_I)} + \mathcal{O}(\eta^2)}{1 + i\eta \frac{\bar{\mathcal{N}}}{2\cos(\theta_I)} + \mathcal{O}(\eta^2)} \left(1 + i\eta \frac{a}{h} \cos(\theta_I) + \mathcal{O}(\eta^2)\right) \\ &= 1 + i\eta \left(\frac{\bar{\mathcal{G}} - \bar{\mathcal{N}}}{2\cos(\theta_I)} + \frac{a}{h} \cos(\theta_I) \right) + \mathcal{O}(\eta^2). \end{aligned} \tag{2.22}$$

This can be summarized as

$$\mathcal{T}(\theta_I, \omega) = 1 + i\eta \mathcal{T}_1(\mathbf{m}_{\text{eff}}, \theta_I) + \mathcal{O}(\eta^2) \tag{2.23}$$

with $\mathcal{T}_1(\mathbf{m}_{\text{eff}}, \theta_I)$ given by

$$\begin{aligned} \mathcal{T}_1(\mathbf{m}_{\text{eff}}, \theta_I) &= -\mathcal{B}_2 \sin(\theta_I) + \frac{\mathcal{C} \sin(\theta_I)^2 - \mathcal{B} \cos(\theta_I)^2 - \mathcal{S}}{2\cos(\theta_I)} + \frac{a}{h} \cos(\theta_I) \\ &= -\mathcal{B}_2 \sin(\theta_I) + \frac{\mathcal{C}^* \sin(\theta_I)^2 - \mathcal{B}^* \cos(\theta_I)^2 - \mathcal{S}^*}{2\cos\theta_I}, \end{aligned} \tag{2.24}$$

where

$$\mathcal{B}^* = \mathcal{B} - a/h, \quad \mathcal{C}^* = \mathcal{C} - a/h, \quad \text{and} \quad \mathcal{S}^* = \mathcal{S} - a/h = \tau^\rho |\Omega_i|. \tag{2.25}$$

The second expression in (2.24), using the coefficients in (2.25), shows that \mathcal{T}_1 does not depend on the choice of the interface thickness a and will be used in Section 4 to slightly simplify the computations.

With the approximation (2.23), it is clear that, at low frequency, $\arg(\mathcal{T})$ changes signs when $\mathcal{T}_1(\mathbf{m}_{\text{eff}}, \theta_I)$ changes signs. This is confirmed in Figures 3c and 3d where the angle for which \mathcal{T}_1 changes signs is denoted by a pink cross and is observed to be very close to both the critical angle observed in numerical simulations and the angle for which the exact value of $\arg(\mathcal{T})$ changes signs at low frequency.

Cancelling the function \mathcal{T}_1 then seems to be a good way to reach the aforementioned effect. Moreover, we will aim at simultaneously maximizing the derivative amplitude $|\partial_\theta \mathcal{T}_1|$ with:

$$\partial_\theta \mathcal{T}_1 = \frac{\partial \mathcal{T}_1}{\partial \theta_I} \tag{2.26}$$

to (i) avoid close-to-zero local minima of $|\mathcal{T}_1|$ without sign change and (ii) “push” the ensuing optimization process towards “stiff” sign changes. For a given critical angle θ_{\min} , these two objectives will be addressed in two ways:

- 320 1. In Section 4, asymptotic closed-form formula of \mathcal{T}_1 and $\partial_\theta \mathcal{T}_1$ obtained for small
 321 elliptic inclusions will be used to obtain “asymptotically optimal” ellipses.
 322 2. In Section 5, a topological optimization algorithm will be proposed to find an
 323 optimal material distribution \mathbf{m}_{opt} in the bounded cell Ω^a that satisfies the
 324 following optimization problem:

$$\begin{aligned}
 & \text{Find} \quad \arg \min_{\mathbf{m}} \tilde{\mathcal{J}}_{\text{main}}(\mathbf{m}) \\
 325 \quad (2.27) \quad & \text{with} \quad \tilde{\mathcal{J}}_{\text{main}}(\mathbf{m}) = \mathcal{J}_{\text{main}}(\mathbf{m}_{\text{eff}}) = \left(\frac{\mathcal{T}_1(\mathbf{m}_{\text{eff}}, \theta_{\text{min}})}{\partial_\theta \mathcal{T}_1(\mathbf{m}_{\text{eff}}, \theta_{\text{min}})} \right)^2.
 \end{aligned}$$

326 In particular, ellipses obtained in the previous step will be used as initiali-
 327 sations. Additional terms will be added to the functional $\mathcal{J}_{\text{main}}$ in (2.27) in
 328 order to reach a given surface ratio between the materials, or to have a suffi-
 329 cient smoothness of the final configuration. The resulting total cost functional
 330 \mathcal{J} will be introduced in Section 5.

331 In both cases, we will rely on the computation of the topological derivatives of the
 332 effective coefficients performed in Section 3 below.

333 *Remark 2.2.* Although the focus is on controlling transmitted energy and on the
 334 related functional (2.27) in this paper, the topological derivatives calculated in Section
 335 3, and the optimization methods described in Section 5 could be used for any other
 336 objective.

337 **3. Topological derivatives of the effective parameters.** In this section,
 338 one aims at describing the sensitivity of the effective parameters to periodic topo-
 339 logical changes of the microstructure, i.e. geometric perturbations of the represen-
 340 tative cell Ω^a . A perturbation is defined as a small inhomogeneity $\mathcal{P}_{\mathbf{z},\varepsilon} = \mathbf{z} + \varepsilon\mathcal{P}$
 341 of size ε , normalized shape \mathcal{P} and physical parameters $(\mu + \Delta\mu, \rho + \Delta\rho)$ intro-
 342 duced at a point $\mathbf{z} \in \Omega^a$. The material perturbation is $\Delta\mathbf{m} = (\Delta\rho, \Delta\mu)$ with
 343 $\Delta\mu > -\min_{\mathbf{y} \in \Omega^a} \mu(\mathbf{y})$ and $\Delta\rho > -\min_{\mathbf{y} \in \Omega^a} \rho(\mathbf{y})$ to satisfy the physical positivity
 344 constraints. The resulting perturbed cell, denoted by $\Omega_{\mathbf{z},\varepsilon}^a$ and represented in Figure
 345 4, features the physical parameters

$$346 \quad (3.1) \quad \mathbf{m}_{\mathbf{z},\varepsilon} := (\mu_{\mathbf{z},\varepsilon}, \rho_{\mathbf{z},\varepsilon}) = (\mu + \Delta\mu \chi_{\mathcal{P}_{\mathbf{z},\varepsilon}}, \rho + \Delta\rho \chi_{\mathcal{P}_{\mathbf{z},\varepsilon}}),$$

347 with $\chi_{\mathcal{P}_{\mathbf{z},\varepsilon}}$ the characteristic function of the perturbation domain $\mathcal{P}_{\mathbf{z},\varepsilon}$.

348 *Remark 3.1.* The definition of $\Delta\mathbf{m}$ may depend on the choice of \mathbf{z} if the unperturbed cell is heterogeneous. However, we disregard the case where the perturbation is located at an interface between two different materials. Consequently, we will drop any dependence of $\Delta\mathbf{m}$ on the space coordinate in the notations, since they do not change the integrals computed hereafter. Moreover, the computation of the topological derivatives are performed for an arbitrary material perturbation $\Delta\mathbf{m}$, as represented in Figure 4. However, in numerical examples we will only consider phase conversion.

356 Let f be a function of the material properties. In this two-dimensional context,
 357 the so-called *topological derivative* of the function f , denoted by $\mathcal{D}f$, is defined thanks
 358 to the following 2D asymptotic expansion:

$$359 \quad (3.2) \quad f_{\mathbf{z},\varepsilon} := f(\mathbf{m}_{\mathbf{z},\varepsilon}) \underset{\varepsilon \rightarrow 0}{=} f(\mathbf{m}) + \varepsilon^2 \mathcal{D}f(\mathbf{m}, \mathbf{z}, \mathcal{P}, \Delta\mathbf{m}) + o(\varepsilon^2).$$

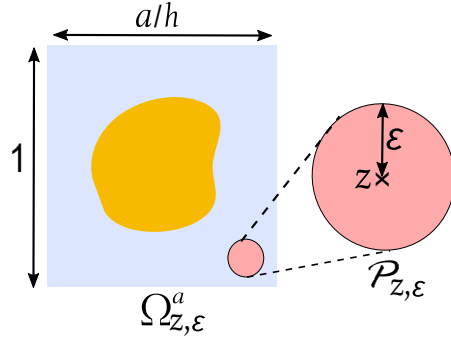


Fig. 4: Cell $\Omega_{z,\varepsilon}^a$ perturbed by the introduction of the inhomogeneity $\mathcal{P}_{z,\varepsilon}$.

360 It describes the influence on the function f of a perturbation located at z , of shape \mathcal{P}
 361 and material perturbation Δm . Therefore, the more negative $\mathcal{D}f(m, z, \mathcal{P}, \Delta m)$ is,
 362 the more efficient such a perturbation at point z would be to decrease f .

363 In this section, the topological derivatives of the effective parameters collected in
 364 (2.15) are computed. First, one looks for an expansion of the solution $\Phi_{z,\varepsilon}$ to the cell
 365 problem (2.10) in the perturbed cell Ω_ε^a in Section 3.1. This allows the computation
 366 of the topological sensitivities of the five effective parameters in Section 3.2.

367 **3.1. Approximation of the perturbed cell problem solution.** To compute
 368 the topological derivatives of the homogenized coefficients, we must characterize the
 369 asymptotic behavior of the cell function Φ in (2.10) when the topological perturbation
 370 (3.1) is introduced. To this end, we first reformulate the cell problem (2.10) into an
 371 integral equation, more suitable for the asymptotic analysis. This analysis is then
 372 pursued formally, i.e. rigorous remainder estimates are not provided. However, such
 373 estimates are given by [14, Proposition 5], and we expect similar arguments to hold
 374 given the similarity between the present cell problem and the one addressed in [14].

375 *Weak forms of the unperturbed and perturbed cell problems.* The first step is to
 376 write the weak form of the cell problem. To do so, we consider a function $v \in H_{\text{per}}^1 =$
 377 $\{u \in H^1(\Omega^a; \mathbb{R}), u \text{ } y_2\text{-periodic}\}$. The first equation of (2.10) is then multiplied by
 378 v and integrated by parts in Ω^a . Using the periodic condition and the boundary
 379 condition in (2.10), one obtains after a division by μ_m :

$$380 \quad (3.3) \quad \mathcal{A}_\mu(\Phi, v) = -\mathbf{F}_\mu(v) + \mathbf{J}(v) \quad \forall v \in H_{\text{per}}^1$$

381 where one has introduced the following functionals for $\mathbf{u} = (u_1, u_2) \in H_{\text{per}}^1 \times H_{\text{per}}^1$
 382 and $v \in H_{\text{per}}^1$:

$$383 \quad (3.4) \quad \begin{cases} \mathcal{A}_\mu(\mathbf{u}, v) = \int_{\Omega^a} \frac{\mu(\mathbf{y})}{\mu_m} \nabla \mathbf{u}(\mathbf{y})^\top \cdot \nabla v(\mathbf{y}) d\mathbf{y} + \mathcal{L}^-(\mathbf{u}, v) + \mathcal{L}^+(\mathbf{u}, v), \\ \mathbf{F}_\mu(v) = \int_{\Omega^a} \frac{\mu(\mathbf{y})}{\mu_m} \nabla v(\mathbf{y}) d\mathbf{y}, \\ \mathbf{J}(v) = \int_I \left[v\left(\frac{a}{2h}, y_2\right) - v\left(-\frac{a}{2h}, y_2\right) \right] e_1 dy_2, \end{cases}$$

384 with

$$385 \quad (3.5) \quad \mathcal{L}^\pm(\mathbf{u}, v) = - \int_I \Lambda \left[\mathbf{u} \left(\pm \frac{a}{2h}, \cdot \right) \right] (y_2) v \left(\pm \frac{a}{2h}, y_2 \right) dy_2.$$

386 The vector-valued weak-formulation (3.3), involving a scalar-valued test function,
387 reflects the two uncoupled problems satisfied by the components (Φ_1, Φ_2) .

388 Similarly, the perturbed field $\Phi_{\mathbf{z},\varepsilon}$ satisfies for all $v \in H^1(\Omega^a; \mathbb{R})$, v y_2 -periodic:

$$389 \quad (3.6) \quad \mathcal{A}_{\mu_{\mathbf{z},\varepsilon}}(\Phi_{\mathbf{z},\varepsilon}, v) = -\mathbf{F}_\mu(v) - \delta\mathbf{F}_{\mathbf{z},\varepsilon}(v) + \mathbf{J}(v),$$

390 with

$$391 \quad (3.7) \quad \delta\mathbf{F}_{\mathbf{z},\varepsilon}(v) = \frac{\Delta\mu}{\mu_m} \int_{\mathcal{P}_{\mathbf{z},\varepsilon}} \nabla v(\mathbf{y}) d\mathbf{y}.$$

392 *Integral equation.* To obtain the integral equation satisfied by $\Phi_{\mathbf{z},\varepsilon}$, one then
393 introduces the Green's function $G(\cdot, \mathbf{x})$ associated with a point source at $\mathbf{x} \in \Omega^a$, i.e.
394 the solution of

$$395 \quad (3.8) \quad \begin{cases} -\nabla_{\mathbf{y}} \cdot \left(\frac{\mu(\mathbf{y})}{\mu_m} \nabla_{\mathbf{y}} G(\mathbf{y}, \mathbf{x}) \right) = \delta(\mathbf{y} - \mathbf{x}) & \forall \mathbf{y} \in \Omega^a, \\ G(\cdot, \mathbf{x}) \text{ } y_2\text{-periodic,} \\ -\mathbf{n} \cdot \nabla_{\mathbf{y}} G(\mathbf{y}, \mathbf{x}) \Big|_{y_1=\pm\frac{a}{2h}} = \Lambda [G(\mathbf{y}, \mathbf{x})] \Big|_{y_1=\pm\frac{a}{2h}} & \forall \mathbf{y} \in I^\pm. \end{cases}$$

396 It can be decomposed as

$$397 \quad (3.9) \quad G(\mathbf{y}, \mathbf{x}) = G_\infty \left(\mathbf{y} - \mathbf{x}; \frac{\mu(\mathbf{x})}{\mu_m} \right) + G_c(\mathbf{y}, \mathbf{x}), \quad \text{with } G_\infty(\mathbf{r}; \mu_*) = -\frac{\ln(\|\mathbf{r}\|)}{2\pi\mu_*},$$

398 where G_∞ is the full-space Green's function solution of the 2D Poisson equation
399 that shares the same singularity as G , and G_c is the complementary part to the
400 Green's function solution accounting for the heterogeneity of the cell and the boundary
401 conditions. Details about these functions are given in Appendix B.

402 For any sufficiently smooth function \mathbf{w} , one gets from (3.8) the integral represen-
403 tation for all $\mathbf{x} \in \Omega^a$:

$$404 \quad (3.10) \quad \mathbf{w}(\mathbf{x}) = \mathcal{A}_\mu(\mathbf{w}, G(\cdot, \mathbf{x}))$$

405 with \mathcal{A}_μ defined in (3.4).

406 Coming back to the perturbed problem, one introduces the surface integral oper-
407 ator $\mathcal{N}_{\mathbf{z},\varepsilon}$:

$$408 \quad (3.11) \quad \mathcal{N}_{\mathbf{z},\varepsilon} \mathbf{f}(\mathbf{x}) = \frac{\Delta\mu}{\mu_m} \int_{\mathcal{P}_{\mathbf{z},\varepsilon}} \nabla \mathbf{f}(\mathbf{y})^\top \cdot \nabla_{\mathbf{y}} G(\mathbf{y}, \mathbf{x}) d\mathbf{y}.$$

409 The choice of piecewise-regular material properties μ ensures the regularity of Φ
410 away from inner interfaces, which in turn allows us to use $\mathbf{w} = \Phi$ in the integral
411 representation (3.10). We can, in addition, set $v = G(\cdot, \mathbf{x})$ in the weak form (3.6)
412 (the resulting integral being defined although $G(\cdot, \mathbf{x})$ does not belong to $H^1(\Omega^a, \mathbb{R})$).
413 Together with the definition (3.4) of \mathcal{A}_μ one obtains:

$$414 \quad (3.12) \quad \begin{aligned} \mathcal{A}_\mu(\Phi_{\mathbf{z},\varepsilon}, G(\cdot, \mathbf{x})) + \mathcal{N}_{\mathbf{z},\varepsilon} \Phi_{\mathbf{z},\varepsilon}(\mathbf{x}) &= -\mathbf{F}_\mu(G(\cdot, \mathbf{x})) - \delta\mathbf{F}_{\mathbf{z},\varepsilon}(G(\cdot, \mathbf{x})) + \mathbf{J}(G(\cdot, \mathbf{x})) \\ &= \mathcal{A}_\mu(\Phi, G(\cdot, \mathbf{x})) - \delta\mathbf{F}_{\mathbf{z},\varepsilon}(G(\cdot, \mathbf{x})), \end{aligned}$$

415 where in the last line we used $v = G(\cdot, \mathbf{x})$ in (3.3). Finally, one considers $\mathbf{w} = \Phi_{z,\varepsilon}$
 416 and $\mathbf{w} = \Phi$ in (3.10). Together with (3.12) this leads to the integral equation satisfied
 417 by the perturbed field $\Phi_{z,\varepsilon}$:

$$418 \quad (3.13) \quad (\mathbf{I} + \mathcal{N}_{z,\varepsilon})(\Phi_{z,\varepsilon})(\mathbf{x}) = \Phi(\mathbf{x}) - \delta \mathbf{F}_{z,\varepsilon}(G(\cdot, \mathbf{x})),$$

419 where the integral operator $\mathcal{N}_{z,\varepsilon}$ and right-hand side term $\delta \mathbf{F}_{z,\varepsilon}(G(\cdot, \mathbf{x}))$ are both
 420 supported by the perturbation domain $\mathcal{P}_{z,\varepsilon}$.

421 *Asymptotic analysis.* Aiming at reformulating the equation (3.13) onto the ref-
 422 erence shape \mathcal{P} , let us introduce the scaled coordinates $\mathbf{x} = \mathbf{z} + \varepsilon \bar{\mathbf{x}}$ and assume the
 423 following expansion, based on previous work [14], for all $\mathbf{x} \in \mathcal{P}_{z,\varepsilon}$:

$$424 \quad (3.14) \quad \Phi_{z,\varepsilon}(\mathbf{x}) = \Phi(\mathbf{z}) + \varepsilon \Phi_1(\bar{\mathbf{x}}) + o(\varepsilon).$$

425 One also writes the following Taylor expansion for the cell function

$$426 \quad (3.15) \quad \Phi(\mathbf{x}) = \Phi(\mathbf{z}) + \varepsilon \bar{\mathbf{x}} \cdot \nabla \Phi(\mathbf{z}) + o(\varepsilon).$$

427 Inserting (3.14) and (3.15) in (3.13) and keeping only the leading and first-order terms
 428 yield:

$$429 \quad (3.16) \quad (\mathbf{I} + \mathcal{N}_{z,\varepsilon}) \left(\varepsilon \Phi_1 \left(\frac{\cdot - \mathbf{z}}{\varepsilon} \right) \right) (\mathbf{x}) = \varepsilon \bar{\mathbf{x}} \cdot \nabla \Phi(\mathbf{z}) - \delta \mathbf{F}_{z,\varepsilon}(G(\cdot, \mathbf{x})),$$

430 since $\mathcal{N}_{z,\varepsilon} \Phi(\mathbf{z}) = \mathbf{0}$. As developed in Appendix B, ∇G_∞ is homogeneous of degree -1
 431 (see (B.1)) and $\nabla G_c(\cdot, \mathbf{x})$ is regular in the neighborhood of \mathbf{z} (see (B.5)). The function
 432 G in (3.8) then satisfies:

$$433 \quad (3.17) \quad \nabla_{\mathbf{y}} G(\mathbf{y}, \mathbf{x}) = \varepsilon^{-1} \nabla G_\infty \left(\bar{\mathbf{y}} - \bar{\mathbf{x}}; \frac{\mu(\mathbf{z})}{\mu_m} \right) + o(\varepsilon^{-1}).$$

434 Inserting the above expansion in (3.16), performing a change of variables to rewrite
 435 the integral on \mathcal{P} and identifying the leading-order ($O(\varepsilon)$) contributions then leads to
 436 the scaled integral equation:

$$437 \quad (3.18) \quad (\mathbf{I} + \mathcal{M})(\tilde{\Phi}_1)(\bar{\mathbf{x}}) = \bar{\mathbf{x}} \cdot (\nabla \Phi(\mathbf{z}) + \mathbf{I}),$$

438 with $\tilde{\Phi}_1(\bar{\mathbf{x}}) = \Phi_1(\bar{\mathbf{x}}) + \bar{\mathbf{x}}$ and \mathcal{M} defined by

$$439 \quad (3.19) \quad \mathcal{M} \mathbf{f}(\bar{\mathbf{x}}) = \frac{\Delta \mu}{\mu_m} \int_{\mathcal{P}} \nabla \mathbf{f}(\bar{\mathbf{y}})^\top \cdot \nabla G_\infty \left(\bar{\mathbf{y}} - \bar{\mathbf{x}}; \frac{\mu(\mathbf{z})}{\mu_m} \right) d\bar{\mathbf{y}}.$$

440 Consequently, introducing \mathbf{R} , the vector solution of the equation:

$$441 \quad (3.20) \quad (\mathbf{I} + \mathcal{M})\mathbf{R}(\bar{\mathbf{x}}) = \bar{\mathbf{x}}$$

442 i.e. the solution to a free-space transmission problem associated with a perturbation
 443 $(\mathcal{P}, \Delta \mu)$, with an homogeneous background of modulus $\mu(\mathbf{z})$, then $\tilde{\Phi}_1$ is given by:

$$444 \quad (3.21) \quad \tilde{\Phi}_1(\bar{\mathbf{x}}) = \mathbf{R}(\bar{\mathbf{x}}) \cdot (\nabla \Phi(\mathbf{z}) + \mathbf{I}).$$

445 Finally, one inserts this in (3.14) to get the first-order expansion:

$$446 \quad (3.22) \quad \Phi_{z,\varepsilon}(\mathbf{x}) = \Phi(\mathbf{z}) + \varepsilon (\mathbf{R}(\bar{\mathbf{x}}) \cdot (\nabla \Phi(\mathbf{z}) + \mathbf{I}) - \bar{\mathbf{x}}) + o(\varepsilon).$$

447 **3.2. Calculation of the topological derivatives.** The results of this section
448 are summarized in the following proposition:

449 *Proposition 3.2.* The topological derivatives of the effective coefficients $\mathcal{S}, \mathcal{B}, \mathcal{C}$,
450 for a material perturbation $(\Delta\mu, \Delta\rho)$ supported by the domain $\mathcal{P}_{z,\varepsilon} = z + \varepsilon\mathcal{P}$, are
451 given by :

$$452 \quad (3.23) \quad \mathcal{DS}(\mathbf{m}, z, \mathcal{P}, \Delta\mathbf{m}) = \frac{\Delta\rho}{\rho_m} |\mathcal{P}|,$$

$$453 \quad (3.24) \quad \mathcal{DB}(\mathbf{m}, z, \mathcal{P}, \Delta\mathbf{m}) = -(\nabla\Phi_1(z) + \mathbf{e}_1) \cdot \mathbf{A}(\mathcal{P}, \mu(z), \Delta\mu) \cdot (\nabla\Phi(z) + \mathbf{I}),$$

$$454 \quad (3.25) \quad \mathcal{DC}(\mathbf{m}, z, \mathcal{P}, \Delta\mathbf{m}) = (\nabla\Phi_2(z) + \mathbf{e}_2) \cdot \mathbf{A}(\mathcal{P}, \mu(z), \Delta\mu) \cdot (\nabla\Phi(z) + \mathbf{I}),$$

456 where the so-called polarization tensor \mathbf{A} is defined from the solution \mathbf{R} of the problem
457 (3.20) as

$$458 \quad (3.26) \quad \mathbf{A}(\mathcal{P}, \mu(z), \Delta\mu) = \frac{\Delta\mu}{\mu_m} \int_{\mathcal{P}} \nabla_{\bar{\mathbf{y}}} \mathbf{R}(\bar{\mathbf{y}}) d\bar{\mathbf{y}}.$$

459 *Remark 3.3.* The polarization tensor \mathbf{A} has been used in previous studies [16, 4,
460 14] where it is sometimes derived using layer potentials rather than volume (surface in
461 2D) integral operators (resulting in possibly different prefactors). It is also related to
462 the concentration (or localization) tensor $\mathbb{A} = \int_{\mathcal{P}} \nabla_{\bar{\mathbf{y}}} \mathbf{R}(\bar{\mathbf{y}}) d\bar{\mathbf{y}}$ much used in microme-
463 chanics [40]. It is symmetric and is known analytically for a variety of inclusion shapes
464 \mathcal{P} , see [40]. In particular, for an elliptic perturbation of semiaxes lengths $(1, \gamma)$ along
465 directions $(\mathbf{a}_1, \mathbf{a}_2)$, it is given by:

466

$$467 \quad (3.27) \quad \mathbf{A}(\mathcal{P}, \mu(z), \Delta\mu) = \pi\gamma(\gamma + 1) \frac{\Delta\mu}{\mu_m} \left(\frac{\mathbf{a}_1 \otimes \mathbf{a}_1}{1 + \gamma + \gamma \frac{\Delta\mu}{\mu(z)}} + \frac{\mathbf{a}_2 \otimes \mathbf{a}_2}{1 + \gamma + \frac{\Delta\mu}{\mu(z)}} \right).$$

468 *Remark 3.4.* The topological derivative of a functional f most often involves a
469 *direct field* (here $\mathbf{x} + \Phi$) and an *adjoint field* depending on f , see e.g. [7, 38]. In the
470 present case, the adjoint fields corresponding to coefficients \mathcal{B} and \mathcal{C} would be found
471 to be $-(x_1 + \Phi_1)$ and $x_2 + \Phi_2$, respectively, as seen in the formula of Proposition 3.2,
472 established in a more direct way below.

473 The steps of the proof of Proposition 3.2 are now given.

474 **3.2.1. Computation of \mathcal{DS} .** We first notice that, owing to the definition of \mathcal{S}
475 in (2.12), one has

$$476 \quad (3.28) \quad \mathcal{S}(\mathbf{m}) = \int_{\Omega^a} \frac{\rho(\mathbf{y})}{\rho_m} d\mathbf{y}.$$

477 Consequently, one gets

$$478 \quad (3.29) \quad \mathcal{S}_{z,\varepsilon} = \mathcal{S}(\mathbf{m}) + \int_{\mathcal{P}_{z,\varepsilon}} \frac{\Delta\rho}{\rho_m} d\mathbf{y} = \mathcal{S}(\mathbf{m}) + \varepsilon^2 \frac{\Delta\rho}{\rho_m} |\mathcal{P}|$$

479 which yields by identification with (3.2) the following result

$$480 \quad (3.30) \quad \mathcal{DS}(\mathbf{m}, z, \mathcal{P}, \Delta\mathbf{m}) = \frac{\Delta\rho}{\rho_m} |\mathcal{P}|.$$

481 **3.2.2. Computation of \mathcal{DB} .** From the expression (2.13), the effective parame-
482 ter $\mathcal{B}_{\mathbf{z},\varepsilon}$ associated with the perturbed cell reads

$$483 \quad (3.31) \quad \mathcal{B}_{\mathbf{z},\varepsilon} = \mathcal{B}(\mathbf{m}) + \int_I \left[\delta\Phi_{\mathbf{z},\varepsilon} \left(\frac{a}{2h}, y_2 \right) - \delta\Phi_{\mathbf{z},\varepsilon} \left(-\frac{a}{2h}, y_2 \right) \right] dy_2,$$

484 with the perturbation for the solution of the cell problem $\delta\Phi_{\mathbf{z},\varepsilon}$ defined by

$$485 \quad (3.32) \quad \delta\Phi_{\mathbf{z},\varepsilon} = \Phi_{\mathbf{z},\varepsilon} - \Phi.$$

486 The left-hand side of (3.6) reads

$$487 \quad (3.33) \quad \mathcal{A}_{\mu_{\mathbf{z},\varepsilon}}(\Phi_{\mathbf{z},\varepsilon}, v) = \mathcal{A}_\mu(\Phi, v) + \mathcal{A}_\mu(\delta\Phi_{\mathbf{z},\varepsilon}, v) + \frac{\Delta\mu}{\mu_{\mathbf{m}}} \int_{\mathcal{P}_{\mathbf{z},\varepsilon}} \nabla\Phi_{\mathbf{z},\varepsilon}(\mathbf{y})^\top \cdot \nabla v(\mathbf{y}) d\mathbf{y}.$$

488 Inserting this equation in (3.6) and using (3.3), one gets for all $v \in H_{\text{per}}^1$:

$$489 \quad (3.34) \quad \mathcal{A}_\mu(\delta\Phi_{\mathbf{z},\varepsilon}, v) + \frac{\Delta\mu}{\mu_{\mathbf{m}}} \int_{\mathcal{P}_{\mathbf{z},\varepsilon}} \nabla\Phi_{\mathbf{z},\varepsilon}(\mathbf{y})^\top \cdot \nabla v(\mathbf{y}) d\mathbf{y} = -\delta\mathbf{F}_{\mathbf{z},\varepsilon}(v).$$

490 Furthermore, $\beta = \Phi_1 + y_1$ satisfies for all $\mathbf{w} \in H^1(\Omega^a; \mathbb{R}^2)$, \mathbf{w} y_2 -periodic

$$491 \quad (3.35) \quad \mathcal{A}_\mu(\mathbf{w}, \beta) = \int_I \left[\mathbf{w} \left(\frac{a}{2h}, y_2 \right) - \mathbf{w} \left(-\frac{a}{2h}, y_2 \right) \right] dy_2.$$

492 Taking $v = \beta$ in (3.34) and $\mathbf{w} = \delta\Phi_{\mathbf{z},\varepsilon}$ in (3.35), the expansion (3.31) reads

$$493 \quad (3.36) \quad \mathcal{B}_{\mathbf{z},\varepsilon} = \mathcal{B}(\mathbf{m}) - \frac{\Delta\mu}{\mu_{\mathbf{m}}} \int_{\mathcal{P}_{\mathbf{z},\varepsilon}} \nabla\beta(\mathbf{y}) \cdot (\nabla\Phi_{\mathbf{z},\varepsilon}(\mathbf{y}) + \mathbf{I}) d\mathbf{y}.$$

494 Consequently, one looks for an asymptotic expansion for $\nabla\Phi_{\mathbf{z},\varepsilon}$. For this purpose, one
495 uses the final expansion (3.22) of the previous section. One also writes the expansion
496 $\nabla\beta(\mathbf{y}) = \nabla\beta(\mathbf{z}) + o(1)$ for all $\mathbf{y} \in \mathcal{P}_{\mathbf{z},\varepsilon}$ and expresses the integral in the scaled
497 coordinates as

$$498 \quad (3.37) \quad \mathcal{B}_{\mathbf{z},\varepsilon} = \mathcal{B}(\mathbf{m}) - \frac{\Delta\mu}{\mu_{\mathbf{m}}} \int_{\mathcal{P}} \nabla\beta(\mathbf{z}) \cdot \left(\frac{1}{\varepsilon} \nabla\Phi_{\mathbf{z},\varepsilon}(\bar{\mathbf{y}}) + \mathbf{I} \right) \varepsilon^2 d\bar{\mathbf{y}} + o(\varepsilon^2).$$

499 Inserting the expansion (3.22) in the above equation yields

$$500 \quad (3.38) \quad \mathcal{B}_{\mathbf{z},\varepsilon} = \mathcal{B}(\mathbf{m}) - \varepsilon^2 \frac{\Delta\mu}{\mu_{\mathbf{m}}} \nabla\beta(\mathbf{z}) \cdot \int_{\mathcal{P}} \nabla\mathbf{R}(\bar{\mathbf{y}}) d\bar{\mathbf{y}} \cdot (\nabla\Phi(\mathbf{z}) + \mathbf{I}) + o(\varepsilon^2).$$

501 Using the definition the definition $\beta = \Phi_1 + y_1$ and the polarization tensor \mathbf{A}
502 defined by (3.26), the topological derivative of \mathcal{B} reads

$$503 \quad (3.39) \quad \mathcal{DB}(\mathbf{m}, \mathbf{z}, \mathcal{P}, \Delta\mathbf{m}) = -(\nabla\Phi_1(\mathbf{z}) + \mathbf{e}_1) \cdot \mathbf{A}(\mathcal{P}, \mu(\mathbf{z}), \Delta\mu) \cdot (\nabla\Phi(\mathbf{z}) + \mathbf{I}).$$

504 **3.2.3. Computation of \mathcal{DC} .** From the expression (2.14), the effective parame-
505 ter $\mathcal{C}_{\mathbf{z},\varepsilon}$ associated with the perturbed cell reads

$$506 \quad (3.40) \quad \mathcal{C}_{\mathbf{z},\varepsilon} = \mathcal{C}(\mathbf{m}) + \int_{\Omega^a} \frac{\mu(\mathbf{y})}{\mu_{\mathbf{m}}} \frac{\partial\delta\Phi_{\mathbf{z},\varepsilon}}{\partial y_2}(\mathbf{y}) d\mathbf{y} + \frac{\Delta\mu}{\mu_{\mathbf{m}}} \int_{\mathcal{P}_{\mathbf{z},\varepsilon}} \left(\frac{\partial\Phi_{\mathbf{z},\varepsilon}}{\partial y_2}(\mathbf{y}) + \mathbf{e}_2 \right) d\mathbf{y} + o(\varepsilon^2).$$

507 We know that Φ_2 satisfies for all $\mathbf{w} \in H_{\text{per}}^1$

$$508 \quad (3.41) \quad \mathcal{A}_\mu(\mathbf{w}, \Phi_2) = - \int_{\Omega^\alpha} \frac{\mu(\mathbf{y})}{\mu_m} \frac{\partial \mathbf{w}}{\partial y_2}(\mathbf{y}) d\mathbf{y}.$$

509 One takes $v = \Phi_2$ in (3.34) and $\mathbf{w} = \delta\Phi_{\mathbf{z},\varepsilon}$ in (3.41) and gets

$$510 \quad (3.42) \quad \int_{\Omega^\alpha} \frac{\mu(\mathbf{y})}{\mu_m} \frac{\partial \delta\Phi_{\mathbf{z},\varepsilon}}{\partial y_2}(\mathbf{y}) d\mathbf{y} = \frac{\Delta\mu}{\mu_m} \int_{\mathcal{P}_{\mathbf{z},\varepsilon}} \nabla\Phi_2(\mathbf{y}) \cdot (\nabla\Phi_{\mathbf{z},\varepsilon}(\mathbf{y}) + \mathbf{I}) d\mathbf{y},$$

511 which yields

$$512 \quad (3.43) \quad \mathcal{C}_{\mathbf{z},\varepsilon} = \mathcal{C}(\mathbf{m}) + \frac{\Delta\mu}{\mu_m} \int_{\mathcal{P}_{\mathbf{z},\varepsilon}} (\nabla\Phi_2(\mathbf{y}) + \mathbf{e}_2) \cdot (\nabla\Phi_{\mathbf{z},\varepsilon}(\mathbf{y}) + \mathbf{I}) d\mathbf{y} + o(\varepsilon^2).$$

513 Once again, we use the Taylor expansion $\nabla\Phi_2(\mathbf{y}) = \nabla\Phi_2(\mathbf{z}) + o(1)$ for all \mathbf{y} in $\mathcal{P}_{\mathbf{z},\varepsilon}$,
514 the expression of the integral in the scaled coordinates and the expansion (3.22) to
515 get the final expression for the topological derivative

$$516 \quad (3.44) \quad \mathcal{DC}(\mathbf{m}, \mathbf{z}, \mathcal{P}, \Delta\mu) = (\nabla\Phi_2(\mathbf{z}) + \mathbf{e}_2) \cdot \mathbf{A}(\mathcal{P}, \mu(\mathbf{z}), \Delta\mu) \cdot (\nabla\Phi(\mathbf{z}) + \mathbf{I}).$$

517 **3.3. Numerical validation.** To validate numerically the found expressions of
518 the topological derivatives, we can compute the error made by the approximation of
519 $\mathcal{B}_{\mathbf{z},\varepsilon}$ and $\mathcal{C}_{\mathbf{z},\varepsilon}$ by $\mathcal{B} + \varepsilon^2\mathcal{DB}$ and $\mathcal{C} + \varepsilon^2\mathcal{DC}$, respectively. Indeed, due to (3.38) and
520 (3.43), this error should be of order ε^3 at least.

521 One starts with an initial reference configuration ($\varepsilon = 0$), computes numerically
522 the solutions of the cell problems (2.10) (their computation will be briefly described
523 in Section 5.1.1), and thus the values of \mathcal{B} and \mathcal{C} from (2.13) and (2.14). The initial
524 configuration is chosen to be heterogenous in order to avoid simplifications than can
525 occur with a homogeneous medium as reference. More precisely, we choose a homoge-
526 nous medium containing an elliptic inclusion of center $(0,0)$ and semiaxes lengths
527 $(0.32 \text{ m}, 0.1 \text{ m})$, tilted of 45° . The physical parameters are again given in Table 1.
Then one inserts a perturbation in the background matrix at $\mathbf{z} = (-0.26 \text{ m}, 0.24 \text{ m})$.

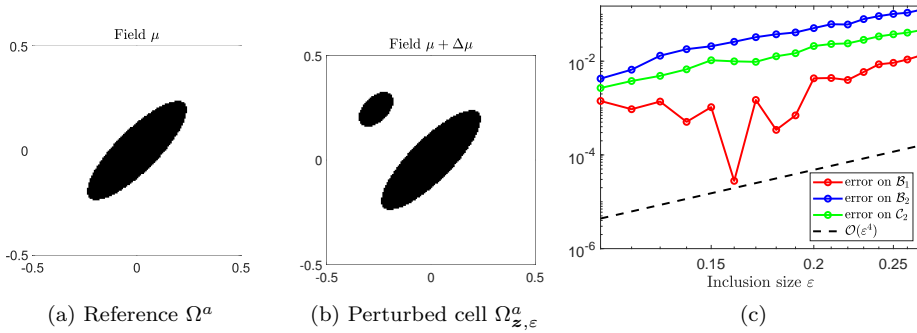


Fig. 5: Test case for an elliptic perturbation: (a) Reference configuration (b) Perturbed configuration for $\varepsilon = 0.1$. (c) Relative error between the exact and approximated effective parameters as a function of ε in a log-log scale.

529 Its physical parameters are the ones of the elliptic inclusion (ρ_i, μ_i) . Its shape is an
 530 ellipse of semiaxes lengths $(\varepsilon, 0.6\varepsilon)$ and tilted of 45° . For $\varepsilon = 0.1$, the configuration is
 531 plotted in Figure 5b. For a given value of ε , one computes the perturbed cell solutions
 532 and thus the exact effective parameters $\mathcal{B}_{\mathbf{z},\varepsilon}$ and $\mathcal{C}_{\mathbf{z},\varepsilon}$ from (2.13) and (2.14). Their
 533 first-order approximations $\mathcal{B} + \varepsilon^2 \mathcal{D}\mathcal{B}$ and $\mathcal{C} + \varepsilon^2 \mathcal{D}\mathcal{C}$ are computed from (3.24) and
 534 (3.25) using (3.27).

535 The relative errors between the exact and approximated values, for instance
 536 $|(\mathcal{B}_1)_{\mathbf{z},\varepsilon} - \mathcal{B}_1 - \varepsilon^2 \mathcal{D}\mathcal{B}_1|/|(\mathcal{B}_1)_{\mathbf{z},\varepsilon}|$, are plotted as functions of the perturbation size
 537 ε in log-log scale in Figure 5c. Since $\mathcal{B}_2 = \mathcal{C}_1$, only one of the corresponding misfits
 538 is represented. The dashed line stands for an error of $\mathcal{O}(\varepsilon^4)$. It seems that this is
 539 the actual order of approximation of the effective parameters, the small variations
 540 for low values of ε being probably due to numerical errors in the computation of the
 541 coefficients. This underlines the fact that the leading order term and consequently
 542 the topological derivatives are well accounted for and that the terms of order ε^3 in the
 543 expansions (3.38) and (3.43) are probably equal to zero for this type of perturbations
 544 with a central symmetry. This was already observed for volume microstructures in
 545 [13, 14], with the intuition that it occurs for perturbations with a central symmetry.
 546 This remains however to be proved. In the case where there is not any central sym-
 547 metry, we therefore expect an error of order $\mathcal{O}(\varepsilon^3)$.

548

549 **4. Approximate parametric optimization in the case of elliptic inclu-**
 550 **sions.** In this section, the topological derivatives are used as tools to analyse the case
 551 of cells made of a unique *elliptic* inclusion Ω_i in a homogenous material. First, the
 552 quality of the approximation of the effective parameters in this case is investigated.
 553 Then, we show that “asymptotically optimal” ellipses can be determined with respect
 554 to the optimization problem presented in Section 2.2.

555 **4.1. Approximation of the effective parameters.** Consider a unique inclu-
 556 sion in an otherwise homogeneous cell, a configuration which can be seen as a single
 557 perturbation in a homogeneous reference cell. In this case, the effective coefficient
 558 $\mathcal{S}^* = \mathcal{S} - a/h$ in (2.25) is given by the exact expression:

$$559 \quad (4.1) \quad \mathcal{S}^* = \varepsilon^2 |\mathcal{P}| \tau^\rho,$$

560 while the topological derivatives formula provide the following approximations:

$$561 \quad (4.2) \quad \mathcal{B}^* = -\varepsilon^2 A_{11} + o(\varepsilon^2), \quad \mathcal{B}_2 = -\varepsilon^2 A_{12} + o(\varepsilon^2), \quad \mathcal{C}^* = \varepsilon^2 A_{22} + o(\varepsilon^2),$$

562 where \mathcal{S}^* , \mathcal{B}^* and \mathcal{C}^* are defined in (2.25).

563 Computing these approximations only requires the knowledge of the polarization
 564 tensor (3.27) for the perturbation shape \mathcal{P} , and the scaling of the result by ε^2 . This
 565 is much less costly than computing numerically the cell solutions and the associated
 566 effective parameters for each choice of inclusion, especially for elliptic inclusions for
 567 which the polarization tensor is known analytically.

568 As an example of the quality of these approximations, we consider an ellipse,
 569 located at $\mathbf{z} = (0, 0)$, of tilted angle $\varphi = 40^\circ$, and semiaxes lengths $(\varepsilon, 0.2\varepsilon)$. In
 570 Figure 6b, the relative errors between the numerically computed value of the effective
 571 parameters through (2.13-2.14) and their approximations given above are represented
 572 for an increasing value of ε . In this case, the reference values themselves decay in
 573 $\mathcal{O}(\varepsilon^2)$ as the **single** inclusion in the cell vanishes. The relative error (e.g. $|(\mathcal{B}^*)_{\mathbf{z},\varepsilon} +$
 574 $\varepsilon^2 A_{11}|/|(\mathcal{B}^*)_{\mathbf{z},\varepsilon}|$), i.e. the ratio between the residual (supposedly in $\mathcal{O}(\varepsilon^4)$ for ellipses)

575 and this reference value is therefore expected to be in $\mathcal{O}(\varepsilon^2)$, which is observed on the
 576 figure. We also observe that a good agreement is obtained even for high values of ε
 577 (i.e. even outside the asymptotic regime). Indeed, for $\varepsilon = 0.5$ (illustrated in Figure
 578 6a) the major axis length is equal to the size of the unit cell and the relative errors
 remain below 15%.

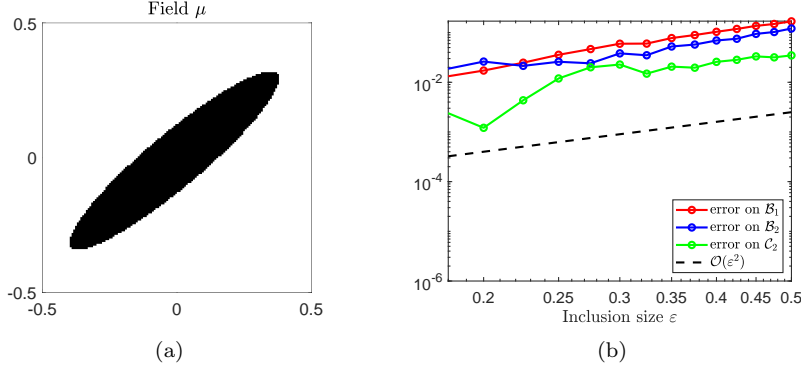


Fig. 6: Test case for an elliptic inclusion: (a) Configuration for $\varepsilon = 0.5$. (b) Relative errors between the exact and approximated effective parameters as functions of inclusion size ε in a log-log scale.

579

580 *Remark 4.1.* The approximation (4.2), using only the polarization tensor computed
 581 from the free-space transmission problem (3.20), is well-known in the domain
 582 of micromechanics as the “dilute” or “Eshelby” approximation (see for instance [40]
 583 and the numerous references therein). It does not account for interactions between
 584 inclusions, and is therefore supposedly restricted to very low concentrations of inclu-
 585 sions, but provides surprisingly accurate results in the present context.

586 Consequently, we propose to use the expressions (4.2) to obtain “optimal” ellipses
 587 that solve the optimization problem presented in Section 2.2.

588 **4.2. Normal incidence: explicit formula and analysis.** When the case
 589 of interest is normal incidence of waves, i.e. when $\theta_I = 0$, closed-form results are
 590 available, that are used in this section as a first example. Indeed, the expression
 591 (2.23) of the function of interest \mathcal{T}_1 is considerably simplified, as

$$592 \quad (4.3) \quad \mathcal{T}_1(\theta_I = 0) = -\frac{1}{2}(\mathcal{B}^* + \mathcal{S}^*) = -\frac{\varepsilon^2}{2}(-A_{11} + \pi\gamma\tau^\rho) + o(\varepsilon^2).$$

593 Then, couples of tilted angle and aspect ratio (φ, γ) for which $\mathcal{T}_1 = o(\varepsilon^2)$ can be found
 594 analytically for given material contrasts (τ^ρ, τ^μ) . Indeed, canceling the leading-order
 595 term above and introducing the expression (3.27) of the polarization tensor gives:

$$596 \quad (4.4) \quad \pi\gamma\tau^\rho = A_{11} \Leftrightarrow \tau^\rho = (1 + \gamma)\tau^\mu \left(\frac{\cos^2(\varphi)}{1 + \gamma + \gamma\tau^\mu} + \frac{\sin^2(\varphi)}{1 + \gamma + \tau^\mu} \right)$$

597 which leads to

$$598 \quad (4.5) \quad \tau^\rho(1 + \gamma + \gamma\tau^\mu)(1 + \gamma + \tau^\mu) - \tau^\mu(1 + \gamma)^2 - (\tau^\mu)^2(1 + \gamma)(\gamma + (1 - \gamma)\cos^2(\varphi)) = 0.$$

599 Therefore, we eventually get

600 (4.6)
$$\begin{cases} \varphi = \arccos \sqrt{\beta} & \text{if } \beta \geq 0 \\ \text{no solution} & \text{if } \beta < 0 \end{cases}, \quad \text{with } \beta = \frac{[\tau^\rho(1 + \gamma + \tau^\mu) - \tau^\mu(1 + \gamma)](1 + \gamma + \gamma\tau^\mu)}{(\tau^\mu)^2(1 - \gamma^2)}.$$

601 This particular solution can be used to check the numerical implementation of \mathcal{T}_1 .

602 As discussed in Section 2.2.3, to find an optimal couple $(\varphi^{\text{opt}}, \gamma^{\text{opt}})$ we also aim at
 603 maximizing the absolute value of the derivative, $|\partial_\theta \mathcal{T}_1(\theta_1 = 0)|$ along the curve defined
 604 by the function (4.6) above. To do so, we rely again on the simplified expression of
 605 the function $\partial_\theta \mathcal{T}_1$ for normal incidence ($\theta_1 = 0$) and on the approximations (4.2) of
 606 the effective coefficients, and use the approximation:

607 (4.7)
$$\begin{aligned} \partial_\theta \mathcal{T}_1(\theta_1 = 0) &= -\mathcal{B}_2 = \varepsilon^2 A_{12} + o(\varepsilon^2) \\ &= \frac{\varepsilon^2 \sin(2\varphi)}{2} \frac{\pi\gamma(1 - \gamma^2)(\tau^\mu)^2}{[1 + \gamma(1 + \tau^\mu)][1 + \gamma + \tau^\mu]} + o(\varepsilon^2). \end{aligned}$$

608 Then plugging the expression (4.6) of φ , one obtains an expression for the leading-
 609 order contribution of $\partial_\theta \mathcal{T}_1$ as a function of γ only, whose maximum is easily found
 610 numerically, as represented in Figure 7.

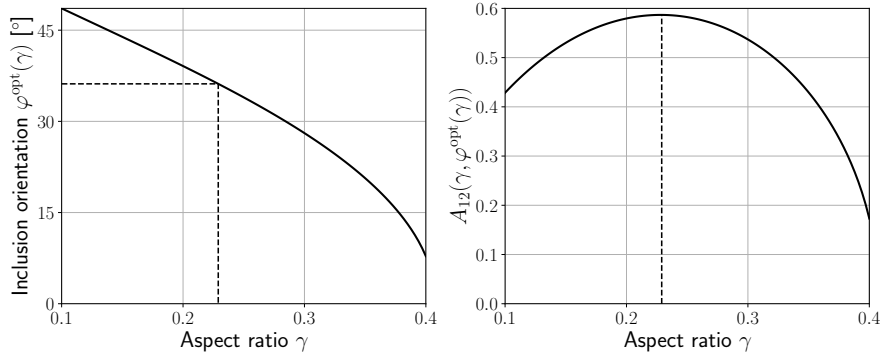


Fig. 7: Left: Curve $\varphi(\gamma)$ corresponding to $\mathcal{T}_1(\theta_1 = 0) = o(\varepsilon^2)$. Right: coefficient A_{12} , i.e. leading-order contribution of $\partial_\theta \mathcal{T}_1(\theta_1 = 0)$, along this curve. Positions of the optimal parameters $(\varphi^{\text{opt}}, \gamma^{\text{opt}})$ are given in dashed lines.

611 Finally, we compute the numerical “true” values of the functions \mathcal{T}_1 and $\partial_\theta \mathcal{T}_1$,
 612 and the cost functional $\mathcal{J}_{\text{main}}$ defined by (2.27), used here as a quality indicator
 613 of a given geometry. For non-vanishing inclusions, of increasing finite size ε , these
 614 quantities are plotted in Figure 8. As expected, the value of \mathcal{T}_1 and therefore the cost
 615 functional $\mathcal{J}_{\text{main}}$ diverge from their asymptotic values as ε increases. Nevertheless,
 616 as summarized in Table 2, the ellipse parametrized by $(\varphi^{\text{opt}}, \gamma^{\text{opt}})$ gives significantly
 617 better results (lower values of \mathcal{T}_1 and $\mathcal{J}_{\text{main}}$) than a disk or an arbitrarily chosen ellipse
 618 with equal surface ratio, also represented in Figure 8.

619 This asymptotic analysis therefore provides a good initial guess that can be used
 620 for topological optimization procedures as seen in the next section.

621 **4.3. Arbitrary incidence: numerical optimum.** For an arbitrary incidence
 622 angle θ_1 , closed-form expressions for an optimal couple such as (4.6) and (4.7) would be

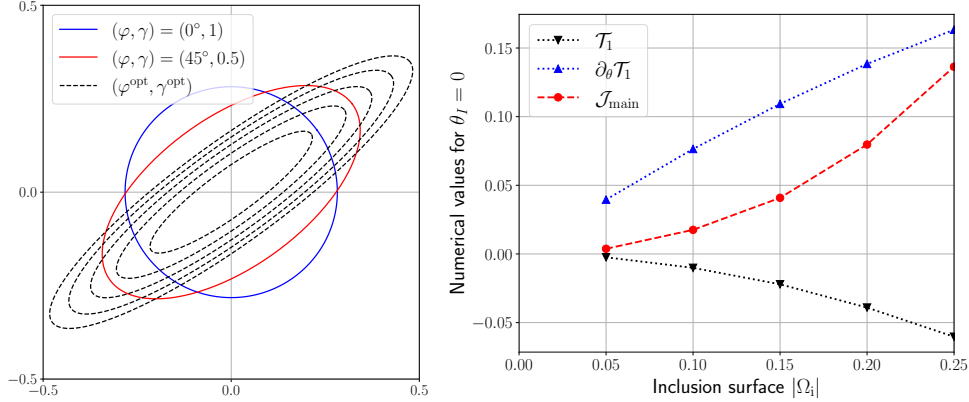


Fig. 8: Left: Investigated ellipses. Test cases with surface $|\Omega_i| = 0.25$ and “optimal” ellipses for normal incidence $\theta_I = 0$ with increasing surfaces $|\Omega_i| \in \{0.05, 0.25\}$. Right: Values of \mathcal{T}_1 , $\partial_\theta \mathcal{T}_1$ and $\mathcal{J}_{\text{main}}$, computed numerically for these “optimal” ellipses.

Ellipse	\mathcal{T}_1	$\partial_\theta \mathcal{T}_1$	$\mathcal{J}_{\text{main}} = (\mathcal{T}_1 / \partial_\theta \mathcal{T}_1)^2$
$(\varphi, \gamma) = (0^\circ, 1)$ (disk)	-0.11	0	\emptyset
$(\varphi, \gamma) = (45^\circ, 0.5)$	-0.10	8.6×10^{-2}	1.4
$(\varphi^{\text{opt}}, \gamma^{\text{opt}}) \approx (36^\circ, 0.23)$	-0.06	0.16	0.14

Table 2: Case $\theta_I = 0$ (normal incidence). Values of functions \mathcal{T}_1 , $\partial_\theta \mathcal{T}_1$ and $\mathcal{J}_{\text{main}}$ for several ellipses with the same surface $|\Omega_i| = 0.25$, see Figure 8. For the disk, one has $\mathcal{B}_2 = 0$ and therefore $\partial_\theta \mathcal{T}_1 = 0$, so that $\mathcal{J}_{\text{main}}$ is not defined.

623 too tedious to obtain. However, the asymptotic approximation of $\mathcal{T}_1(\theta_I)$ as a function
 624 of (φ, γ) can easily be computed numerically.

625 As illustrated in Figures 9 and 10 for $\theta_I = 30^\circ$ and $\theta_I = 45^\circ$, respectively, the
 626 curves (φ, γ) that achieve $\mathcal{T}_1 = o(\varepsilon^2)$ are numerically extracted, the leading-order ap-
 627 proximation of $\partial_\theta \mathcal{T}_1(\theta_I)$ is computed along them, and an optimal couple is determined,
 628 similarly to the case $\theta_I = 0$.

629 For an ellipse with these characteristics and surface $|\Omega_i| = 0.25$, the values of
 630 \mathcal{T}_1 , $\partial_\theta \mathcal{T}_1$ and $\mathcal{J}_{\text{main}}$ are then computed by numerically solving the cell problems,
 631 and compared with the two other ellipses represented in Figure 8. Tables 3 and 4
 632 summarize the results. In these two cases, the “asymptotically optimal” ellipse gives
 633 much better results than the two other test-cases.

Ellipse	\mathcal{T}_1	$\partial_\theta \mathcal{T}_1$	$\mathcal{J}_{\text{main}} = (\mathcal{T}_1 / \partial_\theta \mathcal{T}_1)^2$
$(\varphi, \gamma) = (0^\circ, 1)$ (disk)	-0.11	0.05	4.8
$(\varphi, \gamma) = (45^\circ, 0.5)$	-0.055	0.11	0.26
$(\varphi^{\text{opt}}, \gamma^{\text{opt}}) \approx (52^\circ, 0.34)$	-0.019	0.17	0.012

Table 3: Case $\theta_I = 30^\circ$. Values of functions \mathcal{T}_1 , $\partial_\theta \mathcal{T}_1$ and $\mathcal{J}_{\text{main}}$ for several ellipses with the same surface $|\Omega_i| = 0.25$.

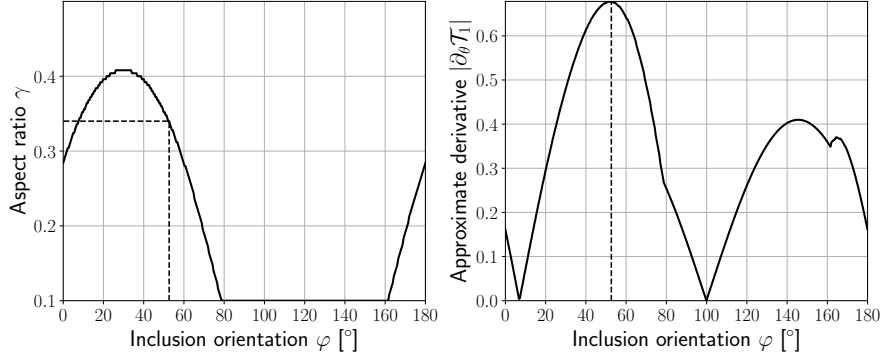


Fig. 9: Case $\theta_1 = 30^\circ$. Couples (φ, γ) that achieve $\mathcal{T}_1 = o(\varepsilon^2)$ (left), corresponding leading-order approximation of $\partial_\theta \mathcal{T}_1$ (right), and numerical extraction of the optimal parameters $(\varphi^{\text{opt}}, \gamma^{\text{opt}}) \approx (53^\circ, 0.34)$ (dashed lines).

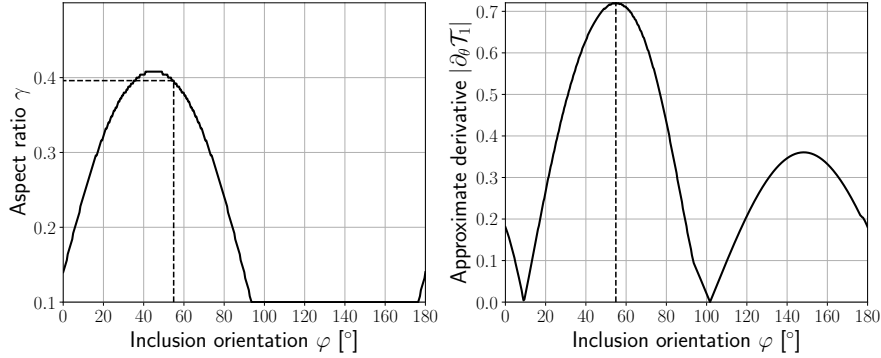


Fig. 10: Case $\theta_1 = 45^\circ$. Couples (φ, γ) that achieve $\mathcal{T}_1 = o(\varepsilon^2)$ (left), corresponding leading-order approximation of $\partial_\theta \mathcal{T}_1$ (right), and numerical extraction of the optimal parameters $(\varphi^{\text{opt}}, \gamma^{\text{opt}}) \approx (55^\circ, 0.40)$ (dashed lines).

Ellipse	\mathcal{T}_1	$\partial_\theta \mathcal{T}_1$	$\mathcal{J}_{\text{main}} = (\mathcal{T}_1 / \partial_\theta \mathcal{T}_1)^2$
$(\varphi, \gamma) = (0^\circ, 1)$ (disk)	-0.11	0.078	1.8
$(\varphi, \gamma) = (45^\circ, 0.5)$	-0.022	0.14	0.025
$(\varphi^{\text{opt}}, \gamma^{\text{opt}}) \approx (55^\circ, 0.4)$	-0.013	0.16	0.0065

Table 4: Case $\theta_1 = 45^\circ$. Values of functions \mathcal{T}_1 , $\partial_\theta \mathcal{T}_1$ and $\mathcal{J}_{\text{main}}$ for several ellipses with the same surface $|\Omega_i| = 0.25$.

634 **5. Topological optimization of microstructured interfaces.** While in the
635 previous section, we used the analytical information given by the topological deriva-
636 tive to analyse the case of a unique elliptic inclusion, the aim in this section is to use
637 the topological derivative in an optimization algorithm to minimize a functional with
638 no *a priori* on the geometry of the inclusion. The efficiency of both methodologies
639 will be investigated through numerical examples in Section 5.3.

640 One aims at generating a microstructure minimizing an objective cost functional
 641 $\mathcal{J}(\mathbf{m}_{\text{eff}})$ composed of both a main function, for example (2.27), and some geometrical
 642 constraints. An optimal microstructure is defined by the phase distribution \mathbf{m}_{opt}
 643 in the bounded cell Ω^a . The cost functional depends on the macroscopic behaviour
 644 which is described by the effective parameters \mathbf{m}_{eff} (2.15) that themselves depend on
 645 \mathbf{m} based on the homogenized model. We therefore consider the following optimization
 646 problem:

$$647 \quad (5.1) \quad \text{Find} \quad \mathbf{m}_{\text{opt}} = \arg \min_{\mathbf{m}} \tilde{\mathcal{J}}(\mathbf{m}) \quad \text{with} \quad \tilde{\mathcal{J}}(\mathbf{m}) = \mathcal{J}(\mathbf{m}_{\text{eff}}).$$

648 In this context, and given the optimization problem (5.1), one looks for the topological
 649 derivative $\mathcal{D}\tilde{\mathcal{J}}$. If \mathcal{J} is differentiable with respect to the effective parameters, $\mathcal{D}\tilde{\mathcal{J}}$ is
 650 computed thanks to the chain rule:

$$651 \quad (5.2) \quad \mathcal{D}\tilde{\mathcal{J}} = \frac{\partial \mathcal{J}}{\partial \mathcal{B}} \mathcal{D}\mathcal{B} + \frac{\partial \mathcal{J}}{\partial \mathcal{B}_2} \mathcal{D}\mathcal{B}_2 + \frac{\partial \mathcal{J}}{\partial \mathcal{S}} \mathcal{D}\mathcal{S} + \frac{\partial \mathcal{J}}{\partial \mathcal{C}_1} \mathcal{D}\mathcal{C}_1 + \frac{\partial \mathcal{J}}{\partial \mathcal{C}} \mathcal{D}\mathcal{C}.$$

652 The final objective is to have at hand a minimization algorithm in order to compute
 653 one optimized material distribution in the sense of (5.1).

654 5.1. Optimization scheme.

655 **5.1.1. FFT-based computation of the cell problems.** In order to perform
 656 topological optimization, multiple computations of the problem (2.10) are required.
 657 Accurately solving this problem with numerical efficiency is therefore crucial. This
 658 problem has been tackled in [18] by (i) reformulating the original problem (A.1)
 659 derived in [30] and posed in an infinite “strip” into the problem (2.10) posed in a
 660 bounded cell (as recalled in Appendix A), and then (ii) decomposing the solution of
 661 this equivalent bounded problem as follows:

$$662 \quad (5.3) \quad \Phi = \Phi_{\text{per}} + \Phi_{\text{bound}}.$$

663 The two terms of this decomposition are

- 664 • The bi-periodic function Φ_{per} that satisfies:

$$665 \quad (5.4) \quad \nabla \cdot (\mu(\mathbf{y}) (\mathbf{I}_2 + \nabla \Phi_{\text{bound}} + \nabla \Phi_{\text{per}})) = \mathbf{0} \text{ in } \Omega^a,$$

666 together with $\int_{\Omega^a} \Phi_{\text{bound}} = 1$ for uniqueness. This is a usual cell problem,
 667 which appears in homogenization of bi-periodic media, with a source term
 668 that is given by $\mathbf{I}_2 + \nabla \Phi_{\text{bound}}$.

- 669 • The boundary corrector Φ_{bound} that is y_2 -periodic and ensures that the
 670 boundary conditions associated to the DtN conditions in (2.10) are satisfied
 671 by imposing:

$$672 \quad (5.5) \quad (\partial_n - \Lambda) \Phi_{\text{bound}} \left(\pm \frac{a}{2h}, \cdot \right) = -(\partial_n - \Lambda) \Phi_{\text{per}} \left(\pm \frac{a}{2h}, \cdot \right).$$

673 The problem is then solved using a fixed-point algorithm specified in [18, Section
 674 3.1] and summarized here for completeness.

- 675 1. Fix $\Phi_{\text{bound}}^{(0)} = \mathbf{0}$.
- 676 2. Step $n \rightarrow n + 1$: given $\Phi_{\text{bound}}^{(n)}$,
 - 677 (a) Compute $\Phi_{\text{per}}^{(n+1)}$ by solving the problem (5.4), with the source term
 678 given by $\Phi_{\text{bound}}^{(n)}$

- 679 (b) Choose a corrector $\Phi_{\text{bound}}^{(n+1)}$ that satisfies (5.5) (an example of choice is
 680 given in [18, Section 3.2])
 681 (c) Compute $\Phi^{(n+1)} = \Phi_{\text{per}}^{(n+1)} + \Phi_{\text{bound}}^{(n+1)}$
 682 3. End when

$$683 \quad (5.6) \quad \frac{\|\Phi^{(n+1)} - \Phi^{(n)}\|_{L^2(\Omega^a)}}{\|\Phi^{(n)}\|_{L^2(\Omega^a)}} < \delta_{\text{FP}}$$

684 with δ_{FP} a user-chosen tolerance.

685 In practice, the fields are discretized on a regular $N_1 \times N_2$ pixel grid mapping
 686 the inner cell Ω^a , and a Fourier-based solver is used for step 2(a), that ensures the
 687 periodicity requirements on the fields and relies on Fast Fourier Transforms (FFT)
 688 for efficiency, following [33]. This algorithm has not been investigated theoretically
 689 but has been observed to converge in practice.

690 **5.1.2. Material updating.** In the configuration mentioned in Introduction,
 691 there are only two phases: Ω_m which is the homogeneous matrix outside the mi-
 692 crostructured array, and $\Omega_i \subset \Omega^a$ which is the inclusion phase. Consequently the only
 693 material modification allowed in the optimization process is a phase conversion from
 694 (ρ_i, μ_i) to (ρ_m, μ_m) or conversely. Accordingly, the material perturbation $\Delta \mathbf{m}$ in the
 695 topological derivatives of Proposition 3.23 is chosen as:

$$696 \quad (5.7) \quad \Delta \mathbf{m} = (\rho_i - \rho_m, \mu_i - \mu_m) \text{ in } \Omega_m \quad \text{and} \quad \Delta \mathbf{m} = (\rho_m - \rho_i, \mu_m - \mu_i) \text{ in } \Omega_i.$$

Moreover, the shape of the perturbation \mathcal{P} is a disk so that the expression of the
 polarization tensor is given by (3.27) with $\gamma = 1$. The use of the boundary corrector
 approach described above requires that the phase at the boundaries $y_1 = \pm \frac{a}{2h}$ is Ω_m .
 Consequently, one defines an optimization domain

$$\Omega^{\text{design}} = [-b; b] \times [-1/2; 1/2] \quad \text{with} \quad b < \frac{a}{2h}$$

697 in which material updates are allowed. Since the material is made of two phases, a
 698 common way to characterize it is to use a *level-set* function Ψ that satisfies:

$$699 \quad (5.8) \quad \begin{cases} \Psi(\mathbf{z}) > 0 & \text{in } \Omega^{\text{design}} \cap \Omega_m \\ \Psi(\mathbf{z}) < 0 & \text{in } \Omega^{\text{design}} \cap \Omega_i \end{cases} \quad \text{and} \quad \|\Psi\|_{L^2(\Omega^{\text{design}})} = 1.$$

700 A projection algorithm introduced in [8] for topological optimization can then be used
 701 [5, 9, 39, 24]. The main steps are recalled in this subsection.

702 First, one defines a signed normalized topological derivative $\overline{\mathcal{D}\mathcal{J}}^{(n)}$ at iteration n as:

$$703 \quad (5.9) \quad \overline{\mathcal{D}\mathcal{J}}^{(n)}(\mathbf{z}) = \begin{cases} \mathcal{D}\mathcal{J}^{(n)}(\mathbf{z}) / \|\mathcal{D}\mathcal{J}^{(n)}\|_{L^2(\Omega^{\text{design}})} & \text{in } \Omega^{\text{design}} \cap \Omega_m \\ -\mathcal{D}\mathcal{J}^{(n)}(\mathbf{z}) / \|\mathcal{D}\mathcal{J}^{(n)}\|_{L^2(\Omega^{\text{design}})} & \text{in } \Omega^{\text{design}} \cap \Omega_i. \end{cases}$$

704 When $\overline{\mathcal{D}\mathcal{J}}^{(n)}$ satisfies the sign condition (5.8), then $\mathcal{D}\mathcal{J}^{(n)}(\mathbf{z}) > 0$ is satisfied in
 705 the whole optimization domain Ω^{design} . Consequently, in this case, the leading-order
 706 approximation of the cost functional \mathcal{J} cannot be decreased anymore by a phase
 707 change in Ω^{design} . Therefore, $\overline{\mathcal{D}\mathcal{J}}^{(n)}$ satisfying (5.8), is a sufficient optimal condition
 708 that ensures that the material configuration corresponds to a local minimum of \mathcal{J} .

709 The iterative updating strategy of [8] for Ψ aims at fulfilling this condition. At each
710 iteration, the new level-set function $\Psi^{(n+1)}$ is computed as:

(5.10)

$$711 \quad \Psi^{(n+1)}(\mathbf{z}) = \frac{1}{\sin(\Theta^{(n)})} \left[\sin((1 - \kappa^{(n)})\Theta^{(n)})\Psi^{(n)}(\mathbf{z}) + \sin(\kappa^{(n)}\Theta^{(n)})\overline{\mathcal{D}\mathcal{J}^{(n)}}(\mathbf{z}) \right],$$

712 with the angle $\Theta^{(n)}$ being defined by the projection

$$713 \quad (5.11) \quad \Theta^{(n)} = \arccos \left(\overline{\mathcal{D}\mathcal{J}^{(n)}}, \Psi^{(n)} \right)_{L^2(\Omega^{\text{design}})}.$$

714 The parameter $\kappa^{(n)}$ in (5.10) is chosen so that the cost functional decreases at each
715 iteration. In practice, it is initialized to $\kappa^{(0)} = 1$ and then at each iteration it is
716 determined down to a minimal value κ_{\min} within an inner optimization loop that
717 reads as:

- 718 1. Initialization to $\kappa^{(n)} = \min(2, \kappa^{(n-1)})$.
- 719 2. Compute $\Psi^{(n+1)}(\mathbf{z})$ using (5.10).
- 720 3. Compute the associated cost functional $\mathcal{J}^{(n+1)}$ (by solving the cell problem
721 and computing relevant effective quantities) and:
 - 722 • if $\mathcal{J}^{(n+1)} < \mathcal{J}^{(n)}$, end step n .
 - 723 • if $\mathcal{J}^{(n+1)} > \mathcal{J}^{(n)}$ and $\kappa^{(n)} > \kappa_{\min}$, set $\kappa^{(n)} = \kappa^{(n)}/2$ and go back to
724 step 2.
 - 725 • if $\mathcal{J}^{(n+1)} > \mathcal{J}^{(n)}$ and $\kappa^{(n)} < \kappa_{\min}$, the whole level-set algorithm is
726 stopped: the cost functional cannot be decreased by the level-set pro-
727 jection.

728 The stopping criterion of the level-set method associated with the updating (5.10)
729 is set as:

$$730 \quad (5.12) \quad |\Theta^{(n)}| < \delta_{\Theta}$$

731 with δ_{Θ} a user-chosen tolerance parameter.

732 *Remark 5.1.* Different initializations are possible for the level-set function $\Psi^{(0)}$.
733 Here we chose to compute it as $f/\|f\|_{L^2(\Omega^{\text{design}})}$ with f being defined by:

$$734 \quad (5.13) \quad f(\mathbf{z}) = \begin{cases} \bar{\mu} - \mu(\mathbf{z}) & \text{if } \mu_{\text{m}} < \mu_{\text{i}}, \\ \mu(\mathbf{z}) - \bar{\mu} & \text{if } \mu_{\text{m}} > \mu_{\text{i}}, \end{cases}$$

735 where $\bar{\mu} = (\mu_{\text{m}} + \mu_{\text{i}})/2$.

736 **5.2. Perimeter and surface constraints.** One may want to reach a given
737 phase ratio in the microstructure. Consequently, we denote by \mathcal{A} the target surface
738 of phase Ω_{i} in the unit cell, and we now consider the following cost functional:

$$739 \quad (5.14) \quad \mathcal{J}_{\text{main}} + \lambda \left(\frac{|\Omega_{\text{i}}|}{\mathcal{A}} - 1 \right)^2$$

740 where we added a penalization term to tend to satisfy the surface condition. The
741 parameter λ is a user-chosen parameter which is chosen so that the final configuration
742 is made of a surface satisfying $|\Omega_{\text{i}}| \in [\mathcal{A} - \mathcal{A}_{\text{err}}; \mathcal{A} + \mathcal{A}_{\text{err}}]$ with \mathcal{A}_{err} also chosen by
743 the user. An augmented Lagrangian strategy [34] could be carried out rather than
744 this quadratic term with a user-controlled parameter λ , but this is beyond the scope
745 of this paper.

746 Furthermore, for manufacturing purposes, one aims at getting smooth final config-
 747 urations that would not be necessary obtained if we only minimize the cost functional
 748 (5.14). Consequently one wants to minimize the following cost functional

$$749 \quad (5.15) \quad \mathcal{J}(\mathbf{m}_{\text{eff}}) = \mathcal{J}_{\text{main}} + \lambda \left(\frac{|\Omega_i|}{\mathcal{A}} - 1 \right)^2 + \alpha_{\text{per}} \text{Per}(\Omega_i)$$

750 with $\text{Per}(\Omega_i) = \int_{\partial\Omega_i} d\sigma$ the perimeter of the inclusions phase in a unit cell and α_{per}
 751 **a user-chosen parameter**. In [6], a regularized perimeter functional Per_ϵ has been in-
 752 troduced to take into account perimeter minimization in topology optimization. This
 753 functional has been proved to converge to the exact perimeter as the regularization
 754 parameter ϵ tends to 0. In practice, the main idea is to solve sequentially the following
 755 approximate problems for $n = 1, \dots, N_{\text{per}}$:

$$756 \quad (5.16) \quad \min \mathcal{J}_{\epsilon_n} := \mathcal{J}_{\text{main}} + \lambda \left(\frac{|\Omega_i|}{\mathcal{A}} - 1 \right)^2 + \alpha_{\text{per}} \text{Per}_{\epsilon_n}(\Omega_i)$$

757 with $\epsilon_{n+1} = \epsilon_n/2$, while ϵ_0 and N_{per} are user-chosen parameters. **In numerical exam-**
 758 **ples, both λ and α_{per} are user-chosen parameters we can play with in order to find**
 759 **a balance between decreasing $\mathcal{J}_{\text{main}}$, satisfying the volume constraint, and getting**
 760 **smooth final configurations (see [46] for comparisons of final configurations with and**
 761 **without perimeter penalization).**

762 **5.3. Numerical examples.** In this section, the desired macroscopic effect is
 763 to minimize the fields along a given direction θ_{min} with (r, θ) the polar coordinates
 764 centered at $\mathbf{X}_{\mathcal{S}} = (-35, 0)$, where the source (2.20) is located. It can be visualized
 765 as minimizing the cumulative energy (2.21) along a given direction θ_{min} . Following the
 766 discussion of Section 2.2.2, we then want to have a change of sign for \mathcal{T}_1 at θ_{min} . We
 767 consequently minimize the regularized cost functional (5.16). The physical parameters
 768 are still the ones typical of steel in concrete given by Table 1, while the numerical
 parameters are given in Table 5.

Table 5: Numerical parameters.

κ_{min}	δ_{Θ}	N_1	N_2	δ_{FP}	ϵ_0	N_{per}
10^{-3}	10^{-1}	101	101	10^{-3}	1	10

769 In a first example, we chose $\theta_1 = 0$ with a surface $\mathcal{A} = 0.2$. In the cost functional
 770 (5.16) the coefficients for the surface penalization λ and the perimeter penalization
 771 α_{per} are chosen so that $\mathcal{A}_{\text{err}} = 0.06$. Their values for each test case is given in Table 6.
 772 Four different initializations are chosen: an ellipse of semi-axes lengths (0.15, 0.3) and
 773 tilted of $-\pi/4$, the same ellipse but tilted of $\pi/4$, a random initialization with the
 774 same ratio of both materials, and the ‘‘asymptotically optimal ellipse’’ computed
 775 in Section 4. The initial configurations, the final configurations obtained after the
 776 optimization process, and the maps of the cumulative energy (2.21) associated with the
 777 effective final configurations are plotted for these four cases in Figure 11. The initial
 778 and final values of the cost functional are also given in Tables 6 and 7, respectively. We
 779 recover the symmetry of the configuration between the first two cases. We observe
 780 that the cost functional is well decreased in every example, so we reach a better
 781 configuration by topological optimization than with the optimal ellipse. In addition,
 782

783 it seems that the number of iterations and the value of the cost functional are smaller
 784 when we initialize by this asymptotically optimal ellipse, so this can be considered as
 785 a valuable initialization to improve the results of the topological optimization process.

786 A second example, for $\theta_I = \pi/4$, $\mathcal{A} = 0.3$ and $\mathcal{A}_{\text{err}} = 0.06$ is described by Table 8,
 787 Table 9 and Figure 12. It confirms that the topological optimization algorithm de-
 788 creases the cost functional. However, for the first two initializations the target angle
 789 of $\pi/4$ does not seem to be reached so accurately, as it can be noticed in Figures 12c
 790 and 12f. In this case, initializing by the optimal ellipse seems even more relevant
 791 since the result obtained in Figure 12i is more satisfying, with a cost functional and a
 792 number of iterations which are lower than for the other initializations. **In both exam-
 793 ples, although the values of $\mathcal{J}_{\text{main}}$ in the end are significantly lower than the starting
 794 ones, the values achieved starting from different initializations are also considerably
 795 different. This is due to the presence of multiple local minima and has already been
 796 observed for the volume case [17]. This therefore underlines the importance of a good
 797 initialization, as the one provided by the optimal ellipse.**

798 Finally, for a better visualization of the optimal periodic microstructures obtained
 799 by repeating the unit cells, four of them are displayed in Figure 13.

Table 6: Initial values for the different configurations with objective $\theta_I = 0$ presented in Figure 11: surface and perimeter parameters, and values of functionals before optimization.

	λ	α_{per}	\mathcal{J} init.	$\mathcal{J}_{\text{main}}$ init.
ellipse (0.15, 0.3, $-\pi/4$)	0.5	0.2	1.21	$9.72 \cdot 10^{-1}$
ellipse (0.15, 0.3, $\pi/4$)	0.5	0.2	1.21	$9.72 \cdot 10^{-1}$
random	0.5	0.2	$5.23 \cdot 10^3$	$5.23 \cdot 10^3$
optimal ellipse	0.15	$5 \cdot 10^{-2}$	$1.02 \cdot 10^{-1}$	$3.61 \cdot 10^{-1}$

Table 7: Final values for the different configurations with objective $\theta_I = 0$ presented in Figure 11: number of iterations, final surface, and values of functionals after optimization.

	N_{iter}	$ \Omega_i $ end	\mathcal{J} end	$\mathcal{J}_{\text{main}}$ end
ellipse (0.15, 0.3, $-\pi/4$)	103	0.15	$2.24 \cdot 10^{-1}$	$1.4 \cdot 10^{-2}$
ellipse (0.15, 0.3, $\pi/4$)	103	0.15	$2.24 \cdot 10^{-1}$	$1.4 \cdot 10^{-2}$
random	82	0.16	$1.93 \cdot 10^{-1}$	$7.2 \cdot 10^{-3}$
optimal ellipse	60	0.14	$6.76 \cdot 10^{-2}$	$2.1 \cdot 10^{-3}$

800 **6. Conclusion.** In this work, formulas are derived for the sensitivities of the
 801 homogenized model that describes the propagation of low-frequency scalar waves
 802 through a row of inclusions embedded in a homogeneous matrix. To do so, we con-
 803 sider asymptotic expansions for a unit cell where a perturbation is introduced. The
 804 expression of the sought topological derivatives of the effective parameters involve the
 805 solution of band cell problems in an unperturbed unit cell, and the usual polarization
 806 tensor. The numerical computation of these band cell problems had been tackled
 807 in a previous work, while the polarization tensor is known analytically for elliptic

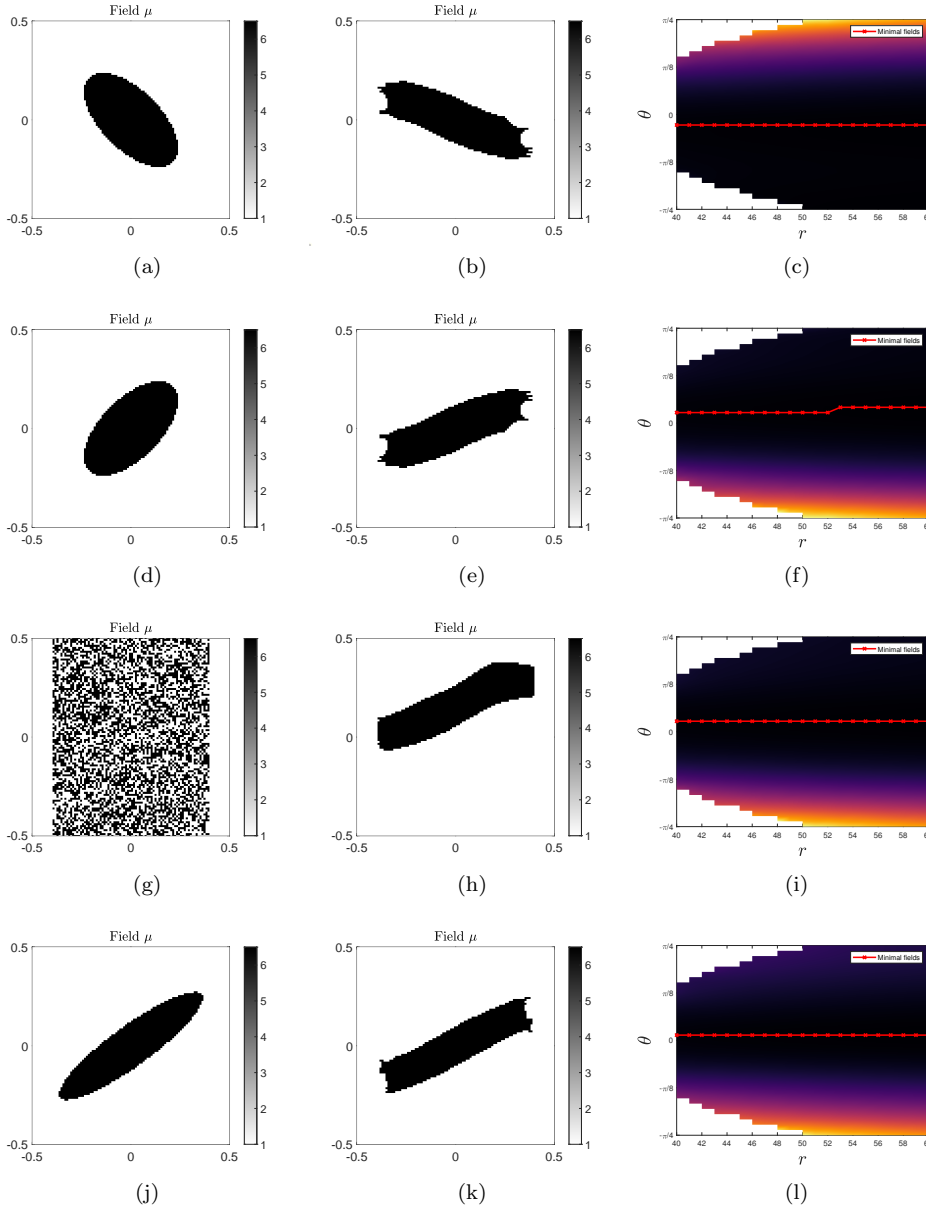


Fig. 11: Test cases for $\theta_1 = 0$ and $\mathcal{A} = 0.2$. From left to right columns: initial configuration, final configuration, and local cumulative energy (2.21) in the effective medium associated to the final configuration where the position of the minimal value for a given r is denoted by the red crosses.

808 perturbations, for example. The expression of the topological derivatives are vali-
 809 dated numerically, and used to perform an analytical analysis of the sensitivity of the
 810 model when considering elliptic inclusions. Then a topological optimization process
 811 is developed to minimize a proposed cost functional, whose objective is to minimize

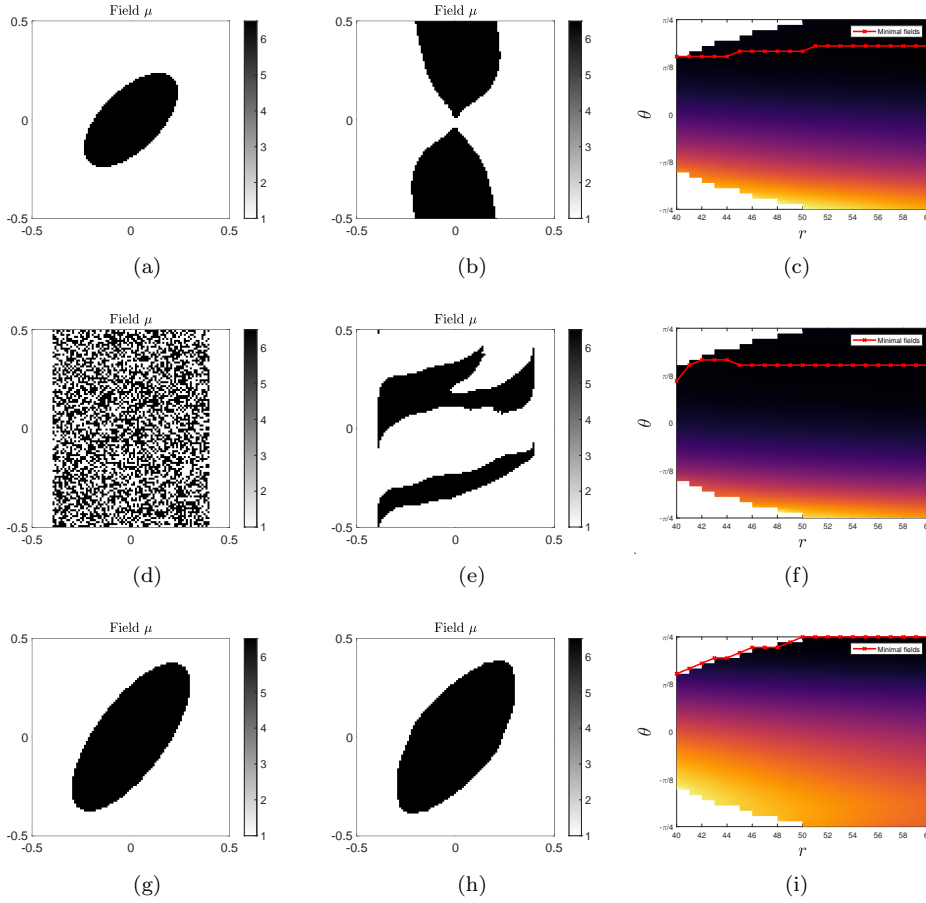


Fig. 12: Test cases for $\theta_I = \pi/4$ and $\mathcal{A} = 0.3$. From left to right columns: initial configuration, final configuration, and local cumulative energy (2.21) in the effective medium associated to the final configuration where the position of the minimal value for a given r is denoted by the red crosses.

812 the transmitted fields along a given direction. The material distribution is updated
 813 at each iteration thanks to a level-set method and using the topological derivatives
 814 obtained in the first part. Surface and perimeter constraints are also added to the
 815 cost functional in order to reach local minima that are smoother and avoid trivial
 816 solutions.

817 This study sets a framework for the optimization of microstructured interfaces
 818 based on their homogenized properties. This work could be extended to other config-
 819 urations, for instance:

- 820 • resonant interfaces, obtained e.g. for highly contrasted inclusions [48, 47].
 821 In this case, frequency-dependent coefficients have been derived, and while
 822 homogenization-based optimization procedures exist for fully periodic reso-
 823 nant media e.g. [49], they are quite scarce for such interfaces, to the best of
 824 our knowledge.

Table 8: Initial values for the different configurations with objective $\theta_I = \pi/4$ presented in Figure 12: surface and perimeter parameters, and values of functionals before optimization.

	λ	α_{per}	\mathcal{J} init.	$\mathcal{J}_{\text{main}}$ init.
ellipse (0.15, 0.3, $\pi/4$)	0.3	$7 \cdot 10^{-2}$	1.51	1.40
random	1	$1 \cdot 10^{-1}$	$2.03 \cdot 10^{-1}$	$2.11 \cdot 10^{-4}$
optimal ellipse	0.3	$7 \cdot 10^{-2}$	$6.27 \cdot 10^{-2}$	$3.30 \cdot 10^{-3}$

Table 9: Final values for the different configurations with objective $\theta_I = \pi/4$ presented in Figure 12: number of iterations, final surface, and values of functionals after optimization.

	N_{iter}	$ \Omega_i $ end	\mathcal{J} end	$\mathcal{J}_{\text{main}}$ end
ellipse (0.15, 0.3, $\pi/4$)	49	0.30	$2.84 \cdot 10^{-2}$	$9.72 \cdot 10^{-5}$
random	52	0.24	$1.35 \cdot 10^{-1}$	$7.99 \cdot 10^{-4}$
optimal ellipse	28	0.28	$2.96 \cdot 10^{-2}$	$8.76 \cdot 10^{-5}$

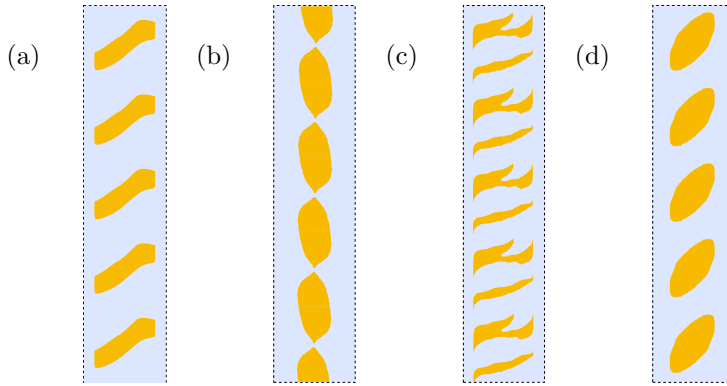


Fig. 13: Final microstructures corresponding to the optimal cells displayed in Figures (a) 11h, (b) 12b, (c) 12e and (d) 12h.

- 825
- high-frequency behavior. Again, the specific homogenization procedure for higher frequencies or shorter wavelengths is well-known for fully periodic media, and has been used for optimization [37], but could be extended to interfaces.
 - 826
 - 827
 - 828
 - 829 • *graded* metasurfaces. By relaxing the periodicity assumption and allowing for slow variations of the periodicity cell size along the interface, one may obtain graded interfaces (sometimes called *quasi-periodic* [41]) able to produce stronger macroscopic effects than their strictly periodic counterparts. Optimization procedures also exist for such configurations [35].
 - 830
 - 831
 - 832
 - 833
 - 834 • other physical contexts. The scalar wave equation addressed in this study is quite general already and may model acoustics, anti-plane shear elastic waves or transversely polarized electromagnetic waves. Extensions to (vector-valued) Maxwell or elasticity equations are however possible within the same
 - 835
 - 836
 - 837

838 matched asymptotics framework, see [43] for a related study, and would open
 839 the way of optimization procedures for macroscopic effects typical of vector-
 840 valued wave problems such as mode conversion at the interface (e.g. P-waves
 841 to S-waves for isotropic elasticity).

842 **Appendix A. Dirichlet-to-Neumann operator.**

843 In this section, the steps used in [18] to obtain the cell problem (2.10) with DtN
 844 boundary conditions are briefly recalled. The problem initially derived in [30], posed
 845 in the infinite strip Ω , reads :

$$846 \quad (A.1) \quad \begin{cases} \nabla \cdot (\mu(\mathbf{y})(\nabla_{\mathbf{y}}\Phi(\mathbf{y}) + \mathbf{I}_2)) = \mathbf{0} \text{ in } \Omega, \\ \mu(\mathbf{y})[\nabla_{\mathbf{y}}\Phi(\mathbf{y}) + \mathbf{I}_2] \cdot \mathbf{n} \text{ and } \Phi \text{ are continuous on } \partial\Omega_i, \\ \Phi \text{ is } y_2\text{-periodic,} \\ \lim_{y_1 \rightarrow \pm\infty} \nabla_{\mathbf{y}}\Phi(y_1, y_2) = \mathbf{0}. \end{cases}$$

847 The variations of the physical parameters are restricted to Ω^a due to its definition
 848 in (2.7). Introducing the half-strips $\Omega_a^+ = [\frac{a}{2h}, +\infty[\times I$ and $\Omega_a^- =]-\infty, -\frac{a}{2h}] \times I$,
 849 see Figure 2, the restrictions $\Phi^\pm := \Phi|_{\Omega_a^\pm}$ satisfy $\Delta\Phi^\pm = \mathbf{0}$ in Ω_a^\pm , along with
 850 the periodicity and decaying conditions. The modal decomposition of these fields,
 851 classically found in the literature on waveguides [26, 15] and also used in [30] to find
 852 approximate solutions, then reads:

$$853 \quad (A.2) \quad \Phi^\pm(y_1, y_2) = \sum_{n \in \mathbb{Z}} \Phi_n^\pm e^{\mp i\xi_n(y_1 \mp \frac{a}{2h})} \Psi_n(y_2), \text{ with } \Psi_n(y_2) = e^{i\xi_n y_2}, \xi_n = 2n\pi.$$

854 The modes $\{\Psi_n\}$ are orthonormal for the L^2 scalar product $(\cdot, \cdot)_I$ on any vertical
 855 section I , i.e. they satisfy:

$$856 \quad (A.3) \quad (\Psi_p, \Psi_q)_I = \delta_{pq}, \text{ with } (f, g)_I := \int_I f(y_2) \overline{g(y_2)} dy_2.$$

857 Consequently, choosing the particular section $I^+ = \{(y_1, y_2) \in \Omega_a^+, y_1 = \frac{a}{2h}\}$, see
 858 Figure 2, yields the expression of the modal coefficients in the right half-strip:

$$859 \quad (A.4) \quad \Phi_n^+ = \left(\Phi^+ \left(\frac{a}{2h}, \cdot \right), \Psi_n \right)_I = \int_I \Phi^+ \left(\frac{a}{2h}, y_2 \right) \overline{\Psi_n(y_2)} dy_2.$$

860 One differentiates the decomposition (A.2) with respect to y_1 and uses the expression
 861 of the coefficients (A.4) to get the following *Dirichlet-to-Neumann* (DtN) operator
 862 linking the traces of Φ and of its normal derivative on the section I^+ where $\Phi = \Phi^+$:

$$863 \quad (A.5) \quad \partial_{y_1} \Phi \left(\frac{a}{2h}, \cdot \right) = \Lambda \left[\Phi \left(\frac{a}{2h}, \cdot \right) \right], \text{ with } \Lambda[f](y_2) = - \sum_{n \in \mathbb{Z}} (f, \Psi_n)_I i\xi_n \Psi_n(y_2).$$

864 Similarly, focusing on the particular section $I^- = \{(y_1, y_2) \in \Omega_a^-, y_1 = -\frac{a}{2h}\}$, see
 865 Figure 2, provides the expression of the “left” modal coefficients of Φ^- . The DtN
 866 relation is finally found to be the same for both interfaces I^\pm , up to the direction of
 867 the outer normal derivative:

$$868 \quad (A.6) \quad \partial_{\mathbf{n}} \Phi \left(\pm \frac{a}{2h}, \cdot \right) = \Lambda \left[\Phi \left(\pm \frac{a}{2h}, \cdot \right) \right], \text{ where } \partial_{\mathbf{n}} = \pm \partial_{y_1}.$$

869 The problem posed in the infinite band (A.1) can thus be rewritten as the problem
870 (2.10) with DtN boundary conditions on the bounded cell (2.7).

871 **Appendix B. Properties of Green's functions.** The definition of the full-
872 space fundamental solution G_∞ in (3.9) implies:

$$873 \quad (\text{B.1}) \quad -\mu_\star \Delta_{\mathbf{r}} G_\infty(\mathbf{r}; \mu_\star) = \delta(\mathbf{r}) \quad \text{and} \quad \nabla_{\mathbf{r}} G_\infty(\mathbf{r}; \mu_\star) = -\frac{\mathbf{r}}{2\pi\mu_\star \|\mathbf{r}\|^2}.$$

874 From the problem (3.8), the decomposition of the fundamental solution G given in
875 (3.9) and the equalities above, then the complementary part G_c is defined as the
876 solution of the PDE:

$$877 \quad (\text{B.2}) \quad \begin{aligned} -\nabla_{\mathbf{y}} \cdot \left(\frac{\mu(\mathbf{y})}{\mu_m} \nabla_{\mathbf{y}} G_c(\mathbf{y}, \mathbf{x}) \right) &= \nabla_{\mathbf{y}} \cdot \left(\frac{\mu(\mathbf{y}) - \mu(\mathbf{x})}{\mu_m} \nabla_{\mathbf{y}} G_\infty \left(\mathbf{y} - \mathbf{x}; \frac{\mu(\mathbf{x})}{\mu_m} \right) \right) \\ &= -\nabla_{\mathbf{y}} \cdot \left(\frac{[\mu(\mathbf{y}) - \mu(\mathbf{x})] (\mathbf{y} - \mathbf{x})}{2\pi\mu(\mathbf{x}) \|\mathbf{y} - \mathbf{x}\|^2} \right) \end{aligned}$$

878 along with the boundary conditions:

$$879 \quad (\text{B.3}) \quad G_c(\cdot, \mathbf{x}) + G_\infty \left(\cdot - \mathbf{x}; \frac{\mu(\mathbf{x})}{\mu_m} \right) \quad \text{is } y_2\text{-periodic,}$$

880 and
(B.4)

$$881 \quad -(\partial_{\mathbf{n}} + \Lambda) [G_c(\mathbf{y}, \mathbf{x})] \Big|_{y_1 = \pm \frac{\sigma}{2h}} = (\partial_{\mathbf{n}} + \Lambda) \left[G_\infty \left(\mathbf{y} - \mathbf{x}; \frac{\mu(\mathbf{x})}{\mu_m} \right) \right] \Big|_{y_1 = \pm \frac{\sigma}{2h}} \quad \forall \mathbf{y} \in I^\pm.$$

882 The right-hand side of the PDE (B.2) is seen to be regular as $\mathbf{y} \rightarrow \mathbf{x}$ as soon as
883 the material coefficient μ is C^1 in a neighborhood of \mathbf{x} . Therefore, $G_c(\cdot, \mathbf{x})$ and its
884 gradient are ensured to be regular functions when \mathbf{x} is itself in the neighborhood of
885 the perturbation point \mathbf{z} , which is not located on a material interface. Using the
886 rescaled coordinates $(\mathbf{y}, \mathbf{x}) = (\mathbf{z} + \varepsilon \bar{\mathbf{y}}, \mathbf{z} + \varepsilon \bar{\mathbf{x}})$, one obtains the asymptotic behavior:

$$887 \quad (\text{B.5}) \quad \nabla_{\mathbf{y}} G_c(\mathbf{y}, \mathbf{x}) = \nabla_{\mathbf{y}} G_c(\mathbf{z}, \mathbf{z}) + o(1) = \mathcal{O}(1) \quad \text{as } \varepsilon \rightarrow 0.$$

888

REFERENCES

- 889 [1] G. ALLAIRE, C. DAPOGNY, AND F. JOUVE, *Shape and topology optimization*, in Geometric
890 Partial Differential Equations - Part II, Elsevier, 2021, pp. 1–132, <https://doi.org/10.1016/bs.hna.2020.10.004>.
891
892 [2] G. ALLAIRE, F. DE GOURNAY, F. JOUVE, AND A.-M. TOADER, *Structural optimization using*
893 *topological and shape sensitivity via a level set method*, Control and Cybernetics, 34 (2005),
894 p. 5980.
895 [3] G. ALLAIRE AND T. YAMADA, *Optimization of dispersive coefficients in the homogenization of*
896 *the wave equation in periodic structures*, Numerische Mathematik, 140 (2018), pp. 265–326,
897 <https://doi.org/10.1007/s00211-018-0972-4>.
898 [4] H. AMMARI AND H. KANG, *Polarization and moment tensors: with applications to inverse*
899 *problems and effective medium theory*, vol. 162, Springer Science & Business Media, 2007.
900 [5] S. AMSTUTZ, *Analysis of a level set method for topology optimization*, Optimization Methods
901 and Software, 26 (2011), pp. 555–573, <https://doi.org/10.1080/10556788.2010.521557>.
902 [6] S. AMSTUTZ, *Regularized perimeter for topology optimization*, SIAM Journal on Control and
903 Optimization, 51 (2013), pp. 2176–2199, <https://doi.org/10.1137/100816997>.
904 [7] S. AMSTUTZ, *An introduction to the topological derivative*, Engineering Computations, 39
905 (2021), pp. 3–33, <https://doi.org/10.1108/ec-07-2021-0433>.

- 906 [8] S. AMSTUTZ AND H. ANDR, *A new algorithm for topology optimization using a level-set method*,
907 Journal of Computational Physics, 216 (2006), pp. 573–588, [https://doi.org/10.1016/j.jcp.](https://doi.org/10.1016/j.jcp.2005.12.015)
908 2005.12.015.
- 909 [9] S. AMSTUTZ, S. M. GIUSTI, A. A. NOVOTNY, AND E. A. DE SOUZA NETO, *Topological derivative*
910 *for multi-scale linear elasticity models applied to the synthesis of microstructures*,
911 International Journal for Numerical Methods in Engineering, 84 (2010), pp. 733–756,
912 <https://doi.org/10.1002/nme.2922>.
- 913 [10] B. ASSOUAR, B. LIANG, Y. WU, Y. LI, J.-C. CHENG, AND Y. JING, *Acoustic metasurfaces*, Nature
914 Reviews Materials, 3 (2018), pp. 460–472, <https://doi.org/10.1038/s41578-018-0061-4>.
- 915 [11] M. P. BENDSOE AND O. SIGMUND, *Topology Optimization*, Springer Berlin Heidelberg, 2003.
- 916 [12] A. BENSOUSSAN, J.-L. LIONS, AND G. PAPANICOLAOU, *Asymptotic analysis for periodic structures*,
917 AMS Chelsea Publishing, 2011.
- 918 [13] M. BONNET, *Higher-order topological sensitivity for 2-d potential problems. Application to*
919 *fast identification of inclusions*, International Journal of Solids and Structures, 46 (2009),
920 pp. 2275 – 2292, <https://doi.org/10.1016/j.ijsolstr.2009.01.021>.
- 921 [14] M. BONNET, R. CORNAGGIA, AND B. B. GUZINA, *Microstructural topological sensitivities of the*
922 *second-order macroscopic model for waves in periodic media*, SIAM Journal on Applied
923 Mathematics, 78 (2018), pp. 2057–2082, <https://doi.org/10.1137/17m1149018>.
- 924 [15] A.-S. BONNET-BEN DHIA AND G. LEGENDRE, *An alternative to Dirichlet-to-Neumann maps*
925 *for waveguides*, Comptes Rendus Mathématique, 349 (2011), pp. 1005–1009, [https://doi.](https://doi.org/10.1016/j.crma.2011.08.006)
926 [org/10.1016/j.crma.2011.08.006](https://doi.org/10.1016/j.crma.2011.08.006).
- 927 [16] D. CEDIO-FENGYA, S. MOSKOW, AND M. VOGELIUS, *Identification of conductivity imperfections*
928 *of small diameter by boundary measurements. continuous dependence and computational*
929 *reconstruction*, Inverse problems, 14 (1998), p. 553, [https://doi.org/10.1088/0266-5611/](https://doi.org/10.1088/0266-5611/14/3/011)
930 [14/3/011](https://doi.org/10.1088/0266-5611/14/3/011).
- 931 [17] R. CORNAGGIA AND C. BELLIS, *Tuning effective dynamical properties of periodic media by*
932 *FFT-accelerated topological optimization*, International Journal for Numerical Methods in
933 Engineering, (2020), <https://doi.org/10.1002/nme.6352>.
- 934 [18] R. CORNAGGIA, M. TOUBOUL, AND C. BELLIS, *FFT-based computation of homogenized interface*
935 *parameters*, Comptes Rendus. Mécanique, 350 (2022), pp. 297–307, [https://doi.org/10.](https://doi.org/10.5802/crmeca.119)
936 [5802/crmeca.119](https://doi.org/10.5802/crmeca.119).
- 937 [19] R. CRASTER, S. GUENNEAU, M. KADIC, AND M. WEGENER, *Mechanical metamaterials*, Reports
938 on Progress in Physics, 86 (2023), p. 094501, <https://doi.org/10.1088/1361-6633/ace069>.
- 939 [20] M. DAVID, C. PIDERI, AND J.-J. MARIGO, *Homogenized interface model describing inho-*
940 *moogeneities located on a surface*, Journal of Elasticity, 109 (2012), p. 153187, [https:](https://doi.org/10.1007/s10659-012-9374-5)
941 [//doi.org/10.1007/s10659-012-9374-5](https://doi.org/10.1007/s10659-012-9374-5).
- 942 [21] B. DELOURME, *Modèles asymptotiques des interfaces fines et périodiques en électromagnétisme*,
943 PhD thesis - Université Pierre et Marie Curie - Paris VI, 2010.
- 944 [22] B. DELOURME, H. HADDAR, AND P. JOLY, *Approximate models for wave propagation across*
945 *thin periodic interfaces*, Journal de mathématiques pures et appliquées, 98 (2012), pp. 28–71.
- 946 [23] B. DELOURME, E. LUNÉVILLE, J.-J. MARIGO, A. MAUREL, J.-F. MERCIER, AND K. PHAM,
947 *A stable, unified model for resonant faraday cages*, Proceedings of the Royal Society A:
948 Mathematical, Physical and Engineering Sciences, 477 (2021), p. 20200668, [https://doi.](https://doi.org/10.1098/rspa.2020.0668)
949 [org/10.1098/rspa.2020.0668](https://doi.org/10.1098/rspa.2020.0668).
- 950 [24] S. GIUSTI, A. FERRER, AND J. OLIVER, *Topological sensitivity analysis in heterogeneous an-*
951 *isotropic elasticity problem. theoretical and computational aspects*, Computer Methods in
952 Applied Mechanics and Engineering, 311 (2016), pp. 134–150, [https://doi.org/10.1016/j.](https://doi.org/10.1016/j.cma.2016.08.004)
953 [cma.2016.08.004](https://doi.org/10.1016/j.cma.2016.08.004).
- 954 [25] S. M. GIUSTI, A. A. NOVOTNY, AND E. A. DE SOUZA NETO, *Sensitivity of the macroscopic*
955 *response of elastic microstructures to the insertion of inclusions*, Proceedings of the Royal
956 Society A: Mathematical, Physical and Engineering Sciences, 466 (2010), pp. 1703–1723,
957 <https://doi.org/10.1098/rspa.2009.0499>.
- 958 [26] I. HARARI, I. PATLASHENKO, AND D. GIVOLI, *Dirichlet-to-Neumann maps for unbounded wave*
959 *guides*, Journal of Computational Physics, 143 (1998), pp. 200–223, [https://doi.org/10.](https://doi.org/10.1006/jcph.1998.5960)
960 [1006/jcph.1998.5960](https://doi.org/10.1006/jcph.1998.5960).
- 961 [27] K. M. HO, C. K. CHENG, Z. YANG, X. X. ZHANG, AND P. SHENG, *Broadband locally resonant*
962 *sonic shields*, Applied Physics Letters, 83 (2003), pp. 5566–5568, [https://doi.org/10.1063/](https://doi.org/10.1063/1.1637152)
963 [1.1637152](https://doi.org/10.1063/1.1637152).
- 964 [28] B. LOMBARD, A. MAUREL, AND J.-J. MARIGO, *Numerical modeling of the acoustic wave prop-*
965 *agation across an homogenized rigid microstructure in the time domain*, Journal of Com-
966 putational Physics, 335 (2017), pp. 558–577, <https://doi.org/10.1016/j.jcp.2017.01.036>.
- 967 [29] J.-J. MARIGO AND A. MAUREL, *Homogenization models for thin rigid structured surfaces and*

- 968 *films*, The Journal of the Acoustical Society of America, 140 (2016), pp. 260–273, <https://doi.org/10.1121/1.4954756>.
- 969
- 970 [30] J.-J. MARIGO, A. MAUREL, K. PHAM, AND A. SBITTI, *Effective dynamic properities of a row*
- 971 *of elastic inclusions: The case of scalar shear waves*, Journal of Elasticity, 128 (2017),
- 972 pp. 265–289, <https://doi.org/10.1007/s10659-017-9627-4>.
- 973 [31] J.-J. MARIGO AND C. PIDERI, *The effective behaviour of elastic bodies containing microcracks*
- 974 *or microholes localized on a surface*, International Journal of Damage Mechanics, SAGE
- 975 Publications, 20 (2011), pp. 1151–1177, <https://doi.org/10.1177/1056789511406914>.
- 976 [32] K. MATSUSHIMA, H. ISAKARI, T. TAKAHASHI, AND T. MATSUMOTO, *A topology optimisation*
- 977 *of composite elastic metamaterial slabs based on the manipulation of far-field behaviours*,
- 978 Structural and Multidisciplinary Optimization, 63 (2020), pp. 231–243, <https://doi.org/10.1007/s00158-020-02689-y>.
- 979
- 980 [33] H. MOULINEC AND P. SUQUET, *A numerical method for computing the overall response of non-*
- 981 *linear composites with complex microstructure*, Computer Methods in Applied Mechanics
- 982 and Engineering, 157 (1998), pp. 69–94, [https://doi.org/10.1016/s0045-7825\(97\)00218-1](https://doi.org/10.1016/s0045-7825(97)00218-1).
- 983 [34] J. NOCEDAL AND S. WRIGHT, *Numerical Optimization (Springer Series in Operations Research*
- 984 *and Financial Engineering)*, Springer, 2006.
- 985 [35] Y. NOGUCHI AND T. YAMADA, *Level set-based topology optimization for graded acoustic meta-*
- 986 *surfaces using two-scale homogenization*, Finite Elements in Analysis and Design, 196
- 987 (2021), p. 103606, <https://doi.org/10.1016/j.finel.2021.103606>.
- 988 [36] Y. NOGUCHI AND T. YAMADA, *Topology optimization of acoustic metasurfaces by using a two-*
- 989 *scale homogenization method*, Applied Mathematical Modelling, 98 (2021), pp. 465–497,
- 990 <https://doi.org/10.1016/j.apm.2021.05.005>.
- 991 [37] Y. NOGUCHI, T. YAMADA, K. IZUL, AND S. NISHIWAKI, *Topology optimization for hyperbolic*
- 992 *acoustic metamaterials using a high-frequency homogenization method*, Computer Methods
- 993 in Applied Mechanics and Engineering, 335 (2018), pp. 419–471, <https://doi.org/10.1016/j.cma.2018.02.031>.
- 994
- 995 [38] A. A. NOVOTNY AND J. SOKOŁOWSKI, *Topological Derivatives in Shape Optimization*, Springer
- 996 Berlin Heidelberg, 2013, <https://doi.org/10.1007/978-3-642-35245-4>.
- 997 [39] J. OLIVER, A. FERRER, J. C. CANTE, S. M. GIUSTI, AND O. LLOBERAS-VALLS, *On multi-scale*
- 998 *computational design of structural materials using the topological derivative*, in *Computational*
- 999 *Methods in Applied Sciences*, Springer International Publishing, sep 2017, pp. 289–
- 1000 308, https://doi.org/10.1007/978-3-319-60885-3_14.
- 1001 [40] W. J. PARNELL, *The Eshelby, Hill, moment and concentration tensors for ellipsoidal inhom-*
- 1002 *ogeneities in the Newtonian potential problem and linear elastostatics*, Journal of Elasticity,
- 1003 (2016), pp. 1–64, <https://doi.org/10.1007/s10659-016-9573-6>.
- 1004 [41] K. PHAM, N. LEBBE, AND A. MAUREL, *Diffraction grating with varying slit width: Quasi-*
- 1005 *periodic homogenization and its numerical implementation*, Journal of Computational
- 1006 Physics, 473 (2023), p. 111727, <https://doi.org/10.1016/j.jcp.2022.111727>.
- 1007 [42] K. PHAM, A. MAUREL, AND J.-J. MARIGO, *Two scale homogenization of a row of locally reso-*
- 1008 *nant inclusions - the case of shear waves*, Journal of the Mechanics and Physics of Solids,
- 1009 106 (2017), pp. 80–94, <https://doi.org/10.1016/j.jmps.2017.05.001>.
- 1010 [43] K. PHAM, A. MAUREL, AND J.-J. MARIGO, *Revisiting imperfect interface laws for two-*
- 1011 *dimensional elastodynamics*, Proceedings of the Royal Society A: Mathematical, Physical
- 1012 and Engineering Sciences, 477 (2021), p. 20200519, <https://doi.org/10.1098/rspa.2020.0519>.
- 1013
- 1014 [44] E. SÁNCHEZ-PALENCIA, *Non-homogeneous media and vibration theory*, Lecture notes in physics,
- 1015 127 (1980).
- 1016 [45] O. SIGMUND, *Materials with prescribed constitutive parameters: An inverse homogenization*
- 1017 *problem*, International Journal of Solids and Structures, 31 (1994), pp. 2313–2329, [https://doi.org/10.1016/0020-7683\(94\)90154-6](https://doi.org/10.1016/0020-7683(94)90154-6).
- 1018
- 1019 [46] M. TOUBOUL, *Acoustic and elastic wave propagation in microstructured media with interfaces:*
- 1020 *homogenization, simulation and optimization*, PhD thesis, Aix-Marseille Universit, 2021.
- 1021 [47] M. TOUBOUL, B. LOMBARD, AND C. BELLIS, *Time-domain simulation of wave propagation*
- 1022 *across resonant meta-interfaces*, Journal of Computational Physics, 414 (2020), p. 109474,
- 1023 <https://doi.org/10.1016/j.jcp.2020.109474>.
- 1024 [48] M. TOUBOUL, K. PHAM, A. MAUREL, J.-J. MARIGO, B. LOMBARD, AND C. BELLIS, *Effective*
- 1025 *resonant model and simulations in the time-domain of wave scattering from a periodic*
- 1026 *row of highly-contrasted inclusions*, Journal of Elasticity, 142 (2020), pp. 53–82, <https://doi.org/10.1007/s10659-020-09789-2>.
- 1027
- 1028 [49] J. VONDŘEJC, E. ROHAN, AND J. HECZKO, *Shape optimization of phononic band gap structures*
- 1029 *using the homogenization approach*, International Journal of Solids and Structures, 113–114

1030

(2017), pp. 147–168, <https://doi.org/10.1016/j.ijsolstr.2017.01.038>.